

Water deuterium fractionation in the high-mass star-forming region G34.26+0.15 based on *Herschel*/HIFI data

A. Coutens,^{1,2★} C. Vastel,^{3,4} U. Hincelin,⁵ E. Herbst,⁵ D. C. Lis,^{6,7} L. Chavarría,⁸
M. Gérin,⁹ F. F. S. van der Tak,^{10,11} C. M. Persson,¹² P. F. Goldsmith¹³ and E. Caux^{3,4}

¹Niels Bohr Institute, University of Copenhagen, Juliane Maries Vej 30, DK-2100 Copenhagen Ø, Denmark

²Centre for Star and Planet Formation, Natural History Museum of Denmark, University of Copenhagen, Øster Voldgade 5-7, DK-1350 Copenhagen K, Denmark

³Université de Toulouse, UPS-OMP, IRAP, F-31028 Toulouse, France

⁴CNRS, Institut de Recherche en Astrophysique et Planétologie, 9 Av. Colonel Roche, BP 44346, F-31028 Toulouse Cedex 4, France

⁵Department of Chemistry, University of Virginia, McCormick Road, Charlottesville, VA 22904, USA

⁶California Institute of Technology, Cahill Center for Astronomy and Astrophysics 301-17, Pasadena, CA 91125, USA

⁷Sorbonne Universités, Université Pierre et Marie Curie, Paris 6, CNRS, Observatoire de Paris, UMR 8112, LERMA, F-75014 Paris, France

⁸Universidad de Chile – CONICYT, Camino del Observatorio 1515, Las Condes, Santiago, Chile

⁹LERMA-LRA, UMR 8112 du CNRS, Observatoire de Paris, Ecole Normale Supérieure, UPMC and UCP, 24 rue Lhomond, F-75231 Paris Cedex 05, France

¹⁰SRON Netherlands Institute for Space Research, Landleven 12, NL-9747 AD Groningen, the Netherlands

¹¹Kapteyn Astronomical Institute, University of Groningen, NL-9700 AV Groningen, the Netherlands

¹²Department of Earth and Space Sciences, Chalmers University of Technology, Onsala Space Observatory, SE-43992 Onsala, Sweden

¹³Jet Propulsion Laboratory, California Institute of Technology, Pasadena, CA 91125, USA

Accepted 2014 September 3. Received 2014 September 3; in original form 2014 April 16

ABSTRACT

Understanding water deuterium fractionation is important for constraining the mechanisms of water formation in interstellar clouds. Observations of HDO and H₂¹⁸O transitions were carried out towards the high-mass star-forming region G34.26+0.15 with the Heterodyne Instrument for the Far-Infrared (HIFI) instrument onboard the *Herschel Space Observatory*, as well as with ground-based single-dish telescopes. 10 HDO lines and three H₂¹⁸O lines covering a broad range of upper energy levels (22–204 K) were detected. We used a non-local thermal equilibrium 1D analysis to determine the HDO/H₂O ratio as a function of radius in the envelope. Models with different water abundance distributions were considered in order to reproduce the observed line profiles. The HDO/H₂O ratio is found to be lower in the hot core ($\sim 3.5 \times 10^{-4}$ – 7.5×10^{-4}) than in the colder envelope ($\sim 1.0 \times 10^{-3}$ – 2.2×10^{-3}). This is the first time that a radial variation of the HDO/H₂O ratio has been found to occur in a high-mass source. The chemical evolution of this source was modelled as a function of its radius and the observations are relatively well reproduced. The comparison between the chemical model and the observations leads to an age of $\sim 10^5$ yr after the infrared dark cloud stage.

Key words: astrochemistry – ISM: abundances – ISM: individual objects: G34.26+0.15 – ISM: molecules.

1 INTRODUCTION

Water, being necessary for the emergence of life, is one of the most important molecules found in space. As a dominant form of oxygen (the most abundant element in the Universe after hydrogen and helium), water controls the chemistry of many other species, whether in the gas phase or in the solid phase (see e.g. the review by van Dishoeck, Herbst & Neufeld 2013). Water is a unique diagnostic of the warmer gas and the energetic processes taking place close to

star-forming regions. Water is also a contributor to maintaining the low temperature of the gas by spectral line radiative cooling. Low temperatures are a requisite for cloud collapse and star formation. Water is mainly in its solid form (as ice on the surface of dust grains) in the cold regions of the interstellar medium as well as in asteroids and comets that likely delivered water to the Earth's oceans (e.g. Hartogh et al. 2011; Alexander et al. 2012). Therefore, constraining the distribution of water vapour and ice during the entire star and planet formation phase is mandatory to understand our own origins.

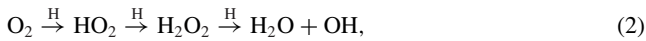
Because of its high abundance in our own atmosphere, observations of interstellar water have been primarily carried out from space observatories including *Infrared Space Observatory (ISO)*, *Spitzer*,

* E-mail: acoutens@nbi.dk

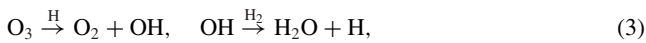
Odin, *Submillimeter Wave Astronomy Satellite (SWAS)*, and recently *Herschel*. Indeed, water has been detected towards the cold pre-stellar core L1544 (Caselli et al. 2012), many low-mass protostars (e.g. Kristensen et al. 2010, 2012; Coutens et al. 2012), high-mass protostars (e.g. Emprechtinger et al. 2013; van der Tak et al. 2013), in the disc of a young star TW Hydrae (Hogerheijde et al. 2011), as well as in many comets (e.g. 103P/Hartley 2: Hartogh et al. 2011; C/2009 P1 (Garradd): Bockelée-Morvan et al. 2012; 45P/Honda-Mrkos-Pajdušáková: Lis et al. 2013) and in asteroids (24 Themis: Campins et al. 2010; Ceres: Küppers et al. 2014). The water abundance shows a very large variation from one source category to another, as well as within each type of sources. The question then arises: how is water produced and why are its abundance variations so large? Although production in the gas phase followed by direct condensation on to dust grains is possible (Bergin, Neufeld & Melnick 1999), observations favour formation through chemical reactions on the surface of cold dust grains. Indeed, in comparison to gas phase water abundance, the observed water ice abundance is too high to be entirely explained by direct accretion from the gas phase (Roberts & Herbst 2002). Consequently surface reactions on cold dust grains to form water molecules have been investigated with modern surface science techniques (e.g. Watanabe & Kouchi 2008). Considering the large reservoir of oxygen and hydrogen atoms in molecular clouds, large amounts of water ice might be produced (Dulieu et al. 2010) following the successive hydrogenation of oxygen on grain surfaces:



Tielens & Hagen (1982) proposed that water ice might also be produced through the successive hydrogenation of molecular oxygen:



demonstrated by Miyauchi et al. (2008), Ioppolo et al. (2008), and Oba et al. (2009), or by hydrogenation of ozone:



demonstrated by Mokrane et al. (2009).

Deuterated water is likely to be formed through the same processes. Many rotational transitions have been detected from the ground, as well as with the *Herschel*/Heterodyne Instrument for the Far-Infrared (HIFI), for example in low-mass protostars (Parise et al. 2005; Liu et al. 2011; Coutens et al. 2012, 2013b; Persson, Jørgensen & van Dishoeck 2013; Persson et al. 2014), high-mass star-forming regions (e.g. Jacq et al. 1990; Gensheimer, Mauersberger & Wilson 1996), and comets (e.g. Bockelée-Morvan et al. 1998; Hartogh et al. 2011; Lis et al. 2013). The HDO/H₂O ratio is an interesting diagnostic tool to help understand the origin of water in the interstellar medium, with a direct comparison with the D/H ratio observed in comets and in the Earth's oceans. It is also helpful to constrain the water formation conditions. In star-forming regions, observations of both high- and low-excitation water lines with a high spectral resolution are needed to disentangle the contributions from the hot cores (or hot corinos in the case of low-mass protostars) and the colder external envelope, that can be linked to the parental cloud, in which stars form. Near protostars, the grain temperature rises above ~100 K, leading to rapid water ice desorption that increases the gas phase H₂O (and its deuterated counterparts) abundance in the inner parts of the envelope. In order to interpret the observed spectra in terms of local physical conditions and relative abundances, radiative transfer modelling is necessary. This is illustrated with the modelling performed by Coutens et al.

(2012, 2013a) towards the low-mass protostar IRAS 16293–2422, where numerous HDO, H₂¹⁸O, and D₂O transitions have been used simultaneously to constrain the abundances in the hot corino, in the cold envelope, and in a water-rich absorbing layer surrounding the envelope.

This paper reports full statistical equilibrium and radiative transfer calculations towards the ultracompact H II region G34.26+0.15 (hereafter G34) using both ground-based observations and *Herschel*/HIFI observations of HDO and the less abundant H₂¹⁸O water isotopologue. The paper is organized as follows. In Sections 2 and 3, we describe the source and the observations, respectively. In Section 4, we present results obtained both with a simple local thermal equilibrium (LTE) modelling and with the 1D non-LTE modelling. In Section 5, we compare them with a chemical model. Finally, we present our conclusions in Section 6.

2 SOURCE DESCRIPTION

Located at a distance of ~3.3 kpc (Kuchar & Bania 1994), G34 has been widely studied in radio continuum (Turner et al. 1974; Reid & Ho 1985; Wood & Churchwell 1989; Sewilo et al. 2011) and radio recombination lines (Garay, Reid & Moran 1985; Garay, Rodriguez & van Gorkom 1986; Gaume, Fey & Claussen 1994; Sewilo et al. 2004, 2011). Several components have been identified in radio continuum observations: two ultracompact H II regions called A and B, a more evolved H II region with a cometary shape (component C), and an extended (1 arcmin) H II region (component D) in the south-east. Chemical surveys were carried out towards the A, B, and C components using single-dish telescopes (MacDonald et al. 1996; Hatchell et al. 1998) and interferometric observations (Mookerjee et al. 2007). Many complex species, characteristic of hot cores, have been detected. From molecular line observations, the emission peak does not coincide with the H II components (Watt & Mundy 1999; De Buizer et al. 2003), but is shifted to the east of the component C by ~1 arcsec (Mookerjee et al. 2007, fig. 3). This difference may arise due to the external influence of the nearby H II regions, or may reveal separate regions of chemical enrichment. The hot core is likely externally heated by stellar photons rather than by shocks, as SiO was not detected at the position of the hot core (Hatchell, Fuller & Millar 2001). This source is also characterized by infall motions as suggested by observations of absorption components of NH₃, CN, HCN, and HCO⁺ (Wyrowski et al. 2012; Liu, Wu & Zhang 2013a; Hajigholi et al., in preparation).

The hot core of G34 has been the target of many *Herschel*/HIFI observations for the past 4 yr, including water line emission (Flagey et al. 2013) and its deuterated counterparts. We present in Section 3 the H₂¹⁸O and HDO transitions observed from the ground as well as the *Herschel*/HIFI observations. Note that the half-power beam width (HPBW) of those telescopes encompasses the components A and B and the molecular peak from component C for all observations.

3 OBSERVATIONS

3.1 Observations and data reduction

This source is part of the Probing Interstellar Molecules with Absorption Line Studies (PRISMAS) Key Program (Gerin et al. 2010) which was followed by an Open Time Program led by C. Vastel. The targeted coordinates are $\alpha(\text{J2000}) = 18^{\text{h}}53^{\text{m}}18^{\text{s}}$, $\delta(\text{J2000}) = 01^{\circ}14'58''$. The observations were performed in the pointed dual beam switch (DBS) mode using the double sideband (DSB) HIFI

Table 1. HDO and H₂¹⁸O transitions observed towards the ultracompact H II region G34^a.

Species	Frequency (GHz)	J_{K_a,K_c}	E_{up}/k (K)	A_{ij} (s ⁻¹)	Telescope	HPBW (arcsec)	F_{eff}	B_{eff}	dv (km s ⁻¹)	rms ^b (mK)	$\int T_{mb} dv$ (K km s ⁻¹)	FWHM (km s ⁻¹)
HDO	80.5783	1 _{1,0} -1 _{1,1}	47	1.32×10^{-6}	IRAM 30-m	31.2	0.95	0.81	0.182	56	2.36	5.9
	225.8967	3 _{1,2} -2 _{2,1}	168	1.32×10^{-5}	IRAM 30-m	11.1	0.92	0.61	0.064	101	10.45	6.7
	241.5616	2 _{1,1} -2 _{1,2}	95	1.19×10^{-5}	IRAM 30-m	10.4	0.90	0.56	0.061	84	12.27	6.6
	464.9245	1 _{0,1} -0 _{0,0}	22	1.69×10^{-4}	CSO	16.5	-	0.35 ^c	0.078	304	7.48	5.2
	490.5966	2 _{0,2} -1 _{1,1}	66	5.25×10^{-4}	HIFI 1a	43.9	0.96	0.76	0.305	10	2.13	7.6
	509.2924	1 _{1,0} -1 _{0,1}	47	2.32×10^{-3}	HIFI 1a	42.3	0.96	0.76	0.294	44	1.76	9.0
	599.9267	2 _{1,1} -2 _{0,2}	95	3.45×10^{-3}	HIFI 1b	35.9	0.96	0.75	0.250	12	2.63	7.7
	848.9618	2 _{1,2} -1 _{1,1}	84	9.27×10^{-4}	HIFI 3a	25.4	0.96	0.75	0.176	10	3.92	10.3
	893.6387	1 _{1,1} -0 _{0,0}	43	8.35×10^{-3}	HIFI 3b	24.1	0.96	0.74	0.167	63	-2.38 ^d	5.9 ^e
	919.3109	2 _{0,2} -1 _{0,1}	66	1.56×10^{-3}	HIFI 3b	23.4	0.96	0.74	0.163	20	2.01	6.1
	p-H ₂ ¹⁸ O	203.4075	3 _{1,3} -2 _{2,0}	204	4.81×10^{-6}	IRAM 30-m	12.1	0.93	0.62	0.074	121	8.38 ^f
p-H ₂ ¹⁸ O ^g	1101.6983	1 _{1,1} -0 _{0,0}	53	1.79×10^{-2}	HIFI 4b	19.2	0.96	0.74	0.136	110	-1.97 ^h	6.4 ⁱ
o-H ₂ ¹⁸ O ^g	547.6764	1 _{1,0} -1 _{0,1}	60	3.29×10^{-3}	HIFI 1a	38.7	0.96	0.75	0.274	12	1.67 ^j	7.5 ^k

Note: ^aThe frequencies, upper energy levels (E_{up}), and Einstein coefficients (A_{ij}) come from the spectroscopic catalogue JPL (Pickett et al. 1998).

^bThe rms is calculated at the spectral resolution of the observations, which is indicated in the column dv .

^cThis value corresponds to the ratio between the main beam efficiency B_{eff} and the forward efficiency F_{eff} .

^dThe integrated flux of the emission component is ~ 0.87 K km s⁻¹, whereas it is ~ -3.25 K km s⁻¹ for the absorbing component.

^eThe full width at half-maximum (FWHM) of the fundamental line at 894 GHz is estimated to be 5.9 km s⁻¹ for the emission component ($v_{LSR} = 58.0$ km s⁻¹) and 3.9 km s⁻¹ for the absorption component ($v_{LSR} = 60.6$ km s⁻¹).

^fAfter subtraction of the CH₃OCH₃ line contaminating the para-H₂¹⁸O line profile.

^gObservations from Flagey et al. (2013).

^hThe integrated flux of the emission component is ~ 1.39 K km s⁻¹, whereas it is ~ -3.36 K km s⁻¹ for the absorbing component.

ⁱThe FWHM of the fundamental H₂¹⁸O line at 1101 GHz is estimated to be 6.4 km s⁻¹ for the emission component ($v_{LSR} = 57.5$ km s⁻¹) and 3.5 km s⁻¹ for the absorption component ($v_{LSR} = 61.2$ km s⁻¹).

^jThe integrated flux of the emission component is ~ 1.80 K km s⁻¹, whereas it is ~ -0.13 K km s⁻¹ for the absorbing component.

^kThe FWHM of the fundamental H₂¹⁸O line at 547 GHz is estimated to be 7.5 km s⁻¹ for the emission component ($v_{LSR} = 57.3$ km s⁻¹) and 3.3 km s⁻¹ for the absorption component ($v_{LSR} = 60.6$ km s⁻¹).

instrument (de Graauw et al. 2010; Roelfsema et al. 2012) onboard the *Herschel Space Observatory* (Pilbratt et al. 2010). The DBS reference positions were situated approximately 3 arcmin east and west of the source. The HIFI Wide Band Spectrometer (WBS) was used with optimization of the continuum, providing a spectral resolution of 1.1 MHz over an instantaneous bandwidth of 4×1 GHz. To disentangle the lines of interest from the lines in the opposite sideband, possibly contaminating our observations, we observed the same transition with three different Local Oscillator (LO) settings. This method is necessary in such chemically rich regions in order to ensure genuine detection of spectral lines. The HDO data were processed using the standard HIFI pipeline up to level 2 with the ESA-supported package HIPE 8.0 (Ott 2010) and were then exported as FITS files into CLASS/GILDAS format¹ for subsequent data reduction. The two linear polarizations were averaged to lower the noise in the final spectrum. The baselines are well fitted by straight lines over the frequency range of the whole band and were subtracted from all observations. The single sideband continuum temperature (that was obtained by dividing by 2 the DSB continuum derived from the linear fit obtained from line-free regions in the spectrum, i.e. assuming a sideband gain ratio of unity) was added to the spectrum of the 1_{1,1}-0_{0,0} fundamental line. To constrain the HDO/H₂O ratio, we also used two H₂¹⁸O transitions observed in the framework of the PRISMAS program and previously published by Flagey et al. (2013). We refer to this paper for the data reduction of these two lines. A list of all the *Herschel*/HIFI observations used in this paper is provided in Table A1.

The ground state 1_{0,1}-0_{0,0} HDO transition was observed at the Caltech Submillimeter Observatory (CSO) in 2011 September using the Fast Fourier Transform Spectrometer (FFTS) with 500 MHz bandwidth. The data were taken under good weather conditions, with 1.5 mm of precipitable water vapour. The beam switching mode has been used with a chop throw of 240 arcsec. The main beam efficiency was determined from total power observations of Mars. The system temperature was about 3500 K during the run. The single sideband continuum temperature (~ 2.2 K) was added to the final baseline-subtracted spectrum.

Three additional HDO transitions at 81 GHz (1_{1,0}-1_{1,1}), 226 GHz (3_{1,2}-2_{2,1}), and 242 GHz (2_{1,1}-2_{1,2}) as well as the ortho-H₂¹⁸O transition at 203 GHz (3_{1,3}-2_{2,0}) were observed with the IRAM 30-m telescope. The observations were carried out in 2011 December using the FFTS at a 50 kHz resolution. The spectral resolution was 0.19, 0.07, and 0.06 km s⁻¹ for the 81, 226, and 242 GHz transitions, respectively. All the observations were performed using the Wobbler Switching mode. The 30 m beam sizes at the observing frequencies are given in Table 1. During this run, weather conditions were good for winter, with 2 mm of precipitable water vapour. System temperatures were always less than 200 K.

Fig. 1 presents the energy level diagram of the HDO transitions used for the modelling. Table 1 summarizes the observations.

3.2 Description of the observations

Most of the observed HDO lines show a Gaussian-like profile (see e.g. Fig. 4). Only the HDO 1_{1,1}-0_{0,0} fundamental transition observed with *Herschel*/HIFI shows an inverse P-Cygni profile, i.e. a profile

¹ <http://www.iram.fr/IRAMFR/GILDAS>

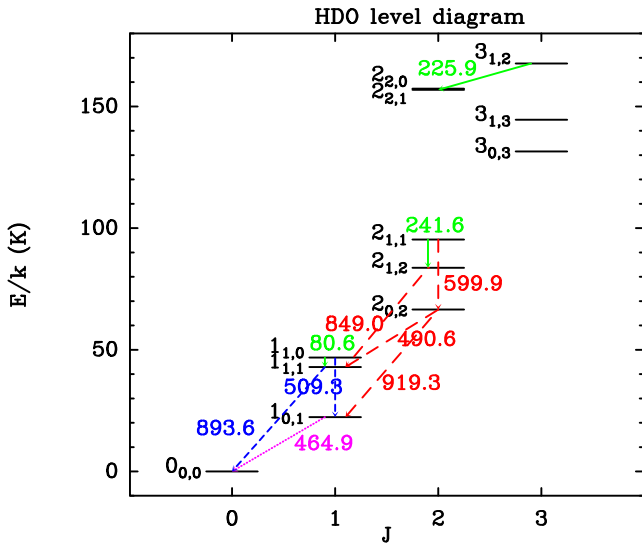


Figure 1. Energy level diagram of the HDO lines. Green solid arrows: the IRAM 30-m observations; blue short dashed arrows: the PRISMAS/HIFI observations; red long dashed arrows: the Open Time HIFI observations; magenta dotted arrow: the CSO observation. The frequencies are given in GHz.

showing a redshifted absorption component and a blueshifted emission component. A similar profile has already been observed for this transition in low-mass protostars (Coutens et al. 2012, 2013b). The Gaussian full width at half-maximum (FWHM) was derived for each line with the *CASSIS*² software (see Table 1). Using the available spectroscopic data bases Cologne Database Molecular Spectroscopy (CDMS; Müller et al. 2001, 2005) and Jet Propulsion Laboratory (JPL; Pickett et al. 1998), we also checked that the different lines are not contaminated by other species. The HDO $2_{1,1}-2_{1,2}$ transition at 242 GHz could be slightly blended with the CH_3COCH_3 $13_{10,4}-12_{9,3}$ line. However a simple LTE modelling of CH_3COCH_3 lines observed in the spectra shows that the contribution of CH_3COCH_3 is negligible. With a column density of $4 \times 10^{16} \text{ cm}^{-2}$, an excitation temperature of 100 K, a FWHM of 6 km s^{-1} , and a source size of 1.7 arcsec, the predicted intensity of the CH_3COCH_3 line at 241.6 GHz is 0.06 K, to be compared with the observed line intensity 1.75 K. The HDO $2_{1,2}-1_{1,1}$ line at 849 GHz is very probably blended with three $^{13}\text{CH}_3\text{OH}$ lines ($18_{3,15}-17_{3,14} \text{ A-}$, $18_{4,14}-17_{4,13} \text{ A+}$, and $18_{4,15}-17_{4,14} \text{ A-}$) lying in the redshifted portion of the line profile. This could explain why this line is broader than the others (see Table 1). As the $^{13}\text{CH}_3\text{OH}$ contribution could be non-negligible, we do not use this HDO line to constrain the abundances. We present however the modelling of this line for completeness. The other HDO lines do not show any potential blending. The portion of the 600 GHz line observed at $v > 72 \text{ km s}^{-1}$ is produced by the CH_3OH $7_{3,5}-6_{2,4} v = 0 \text{ A+}$ line from the image band ($v = 590.3 \text{ GHz}$).

The para- H_2^{18}O $3_{1,3}-2_{2,0}$ line is blended with the CH_3OCH_3 $3_{3,1,1}-2_{2,1,1}$ and $3_{3,0,3}-2_{2,1,3}$ transitions at 203.4101 and 203.4114 GHz ($E_{\text{up}} = 18 \text{ K}$). We can reproduce, with a LTE modelling approach, the CH_3OCH_3 lines observed nearby in the spectra (see Fig. 2) as well as in the other bands. The CH_3OCH_3 lines are well fitted with a column density of $7 \times 10^{17} \text{ cm}^{-2}$, an excitation temperature of 100 K, a FWHM of 6 km s^{-1} , and a source size of 1.7 arcsec.

² <http://cassis.irap.omp.eu>

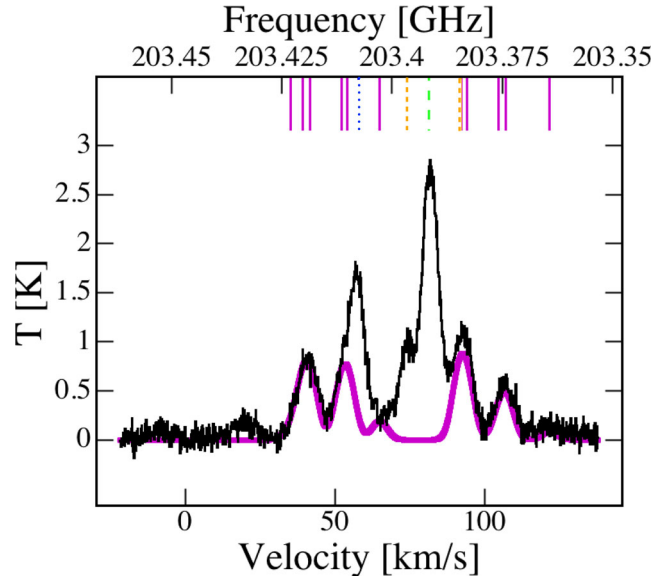


Figure 2. IRAM 30-m observations (in black) of the para- H_2^{18}O $3_{1,3}-2_{2,0}$ transition at 203.4 GHz. The frequency of the H_2^{18}O line is indicated by a blue dotted line ($v = 58 \text{ km s}^{-1}$). The other lines observed in this spectra are the $\text{SO}_2 v = 0$ $12_{0,12}-11_{1,11}$ line at 81.5 km s^{-1} (green long dashed line), the $\text{C}_2\text{H}_5\text{CN} v = 0$ $23_{2,22}-22_{2,21}$ line at 74.1 km s^{-1} (yellow short dashed line), and several CH_3OCH_3 lines (magenta solid lines). A LTE modelling of the CH_3OCH_3 lines (in magenta) was carried out to estimate the contamination of the para- H_2^{18}O line by the CH_3OCH_3 $3_{3,1,1}-2_{2,1,1}$ transition.

The predicted line profiles of the CH_3OCH_3 transitions blended with H_2^{18}O are then subtracted from the observed line profile to extract the proper H_2^{18}O spectrum. Because of the high number of CH_3OCH_3 lines considered in the analysis and the presence of CH_3OCH_3 lines with similar upper energy levels (18 K) around the H_2^{18}O feature (see Fig. 2), the uncertainty produced by this subtraction is negligible with respect to the calibration uncertainty (≤ 20 per cent).

4 RADIATIVE TRANSFER MODELLING

4.1 Rotational diagram analysis

A simple LTE modelling was first employed to estimate the HDO/ H_2O ratio in the hot core. We plot in Fig. 3 the rotation diagram (Goldsmith & Langer 1999) of the HDO lines shown in Table 1. We exclude the fundamental transition at 894 GHz, which shows absorption and probably probes colder regions outside of the hot core. We take into account beam dilution and consider different source sizes between 1 and 5 arcsec, as the exact size of the hot core is unknown. Indeed, the structure determined by van der Tak et al. (2013) predicts a size of 4.5 arcsec for $T > 100 \text{ K}$, whereas the interferometric observations of two HDO lines by Liu et al. (2013b) favour a smaller source size which, however, is not well constrained. No linear curve is in reasonable agreement with the complete data set. Plausible explanations are that the lines are optically thick or that they do not all have the same excitation temperature. We estimate the critical densities of these species using the HDO collisional coefficients with ortho- and para- H_2 of Faure et al. (2012). At $\sim 100 \text{ K}$, the critical densities are about $5 \times 10^6 - 5 \times 10^7 \text{ cm}^{-3}$ for all lines, except for the lines at 80, 226, and 242 GHz that have critical densities between 3×10^4 and $3 \times 10^5 \text{ cm}^{-3}$. These latter lines are at low frequencies, so that their radiative decay is slower. They

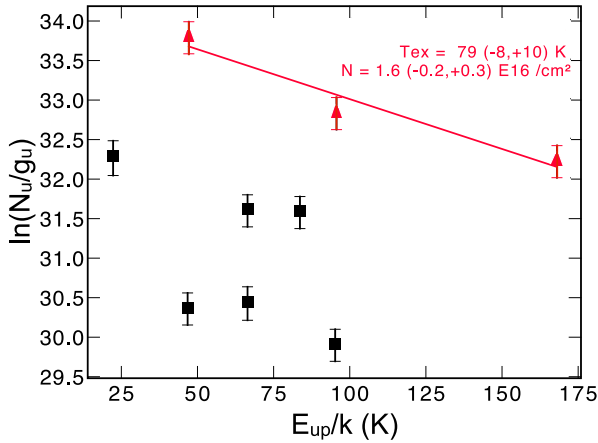


Figure 3. Rotational diagram of the HDO lines. The fundamental line at 894 GHz is excluded from the figure. A source size of 4 arcsec is assumed. The error bars correspond to uncertainties of 20 per cent. A linear fit was made using only the lines with low critical densities (81, 226, and 242 GHz, indicated by red triangles) to estimate the HDO column density ($\sim 1.6 \times 10^{16} \text{ cm}^{-2}$) and the excitation temperature ($\sim 79 \text{ K}$) in the hot core (see text).

are consequently probably in LTE, as the density in the hot core is expected to be $\gtrsim 10^6 \text{ cm}^{-3}$ (van der Tak et al. 2013). In addition, these three lines are also those with the expected lowest opacities. We consequently fit a straight line to these three points only. The column density and the excitation temperature of HDO were then estimated for different values of the source size (1–5 arcsec). To derive the HDO/H₂O ratio, we used the H₂¹⁸O 3_{1,3}–2_{2,0} line observed at 203 GHz with IRAM. Indeed this line is quite excited and its critical density is relatively low, about 10^5 cm^{-3} . Using the same excitation temperature as HDO, we calculated the column density of H₂¹⁸O in the hot core and derived an estimate of the HDO/H₂O ratio between 5.2×10^{-4} and 5.7×10^{-4} . The H₂¹⁶O/H₂¹⁸O ratio is assumed to be 400 following the relation determined by Wilson (1999) between the ¹⁶O/¹⁸O isotopic ratio and the distance of the source from the Galactic centre. The derived HDO/H₂O ratio is consistent with the previous estimates by Jacq et al. (1990, 4×10^{-4}) and Liu et al. (2013b, 3.0×10^{-4}), who assumed an H₂¹⁶O/H₂¹⁸O ratio equal to 500. It is also slightly greater than the estimate by Gensheimer et al. (1996, 1.1×10^{-4}).

4.2 Non-LTE spherical modelling

4.2.1 Model description

Only three HDO lines (among 10) were used to estimate the HDO/H₂O ratio in the hot core with the rotational diagram analysis. We consequently decided to employ non-LTE spherical modelling (that also considers the line opacities) to include the information provided by all the HDO lines (except the 848 GHz line that is probably blended with ¹³CH₃OH) and to determine the water deuterium fractionation in both the hot core and the colder part of the envelope. We used the RATRAN code (Hogerheijde & van der Tak 2000) that assumes spherical symmetry and takes into account continuum emission and absorption by dust. To derive the HDO and H₂¹⁸O abundances, we used the temperature and H₂ density profiles derived by van der Tak et al. (2013, section 4.1). This structure was determined taking into account James Clerk Maxwell Telescope (JCMT)/Submillimetre Common-User Bolometer Array (SCUBA) and Photoconductor Array Camera and Spectrometer (PACS) data.

The radial velocity profile (v_r) and the turbulence width (Doppler b-parameter, db) have also to be provided in RATRAN. We describe in Appendix B2 the method employed to constrain them and show the final v_r and db profiles used in the analysis. We find that inward motions ($v_r \sim -3 \text{ km s}^{-1}$) are present in the cold envelope, while outward motions ($v_r \sim 4 \text{ km s}^{-1}$) take place in the inner regions. The same type of velocity profile was found in SgrB2(M) by Rolffs et al. (2010). The Doppler b-parameter appears lower in the inner regions ($db \sim 2.0 \text{ km s}^{-1}$) than in the outer regions ($db \sim 2.5 \text{ km s}^{-1}$), similarly to what was found by Caselli & Myers (1995) and Herpin et al. (2012) in other high-mass sources. To reproduce the continuum levels seen in the observations as best as possible, we used the dust opacities from Ossenkopf & Henning (1994), with thick ice mantles and a gas density of 10^6 cm^{-3} . The dust opacities used by van der Tak et al. (2013, thin ices mantles with gas density of 10^6 cm^{-3}) to derive the structure would not however differ too much, as the predicted continuum is consistent with the observations to within 10–20 per cent uncertainties. The most recent HDO and H₂¹⁸O collisional coefficients calculated with ortho- and para-H₂ by Faure et al. (2012) and Daniel, Dubernet & Grosjean (2011), respectively, were used. The ortho/para ratio of H₂ is assumed to be at LTE in each cell of the envelope. It consequently varies from $\sim 10^{-2}$ in the coldest regions up to the equilibrium value of 3 in the warm regions.

4.2.2 Modelling of the HDO lines with an abundance jump

Most of the studies of water and deuterated water in star-forming regions (e.g. Ceccarelli et al. 2000; Parise et al. 2005; van der Tak et al. 2006; Coutens et al. 2012; Herpin et al. 2012) assume an abundance jump at $T_j = 100 \text{ K}$, corresponding to the temperature at which the water molecules are supposed to be released in the gas phase by thermal desorption. In a first step, we consequently assumed such an abundance jump for the modelling of the HDO lines. According to the physical structure used here (van der Tak et al. 2013), the source size corresponding to $T > 100 \text{ K}$ is ~ 4.5 arcsec (diameter). We ran a grid of models with various inner ($T > 100 \text{ K}$) and outer ($T < 100 \text{ K}$) abundances and realized that, regardless of the velocity profiles, the intensities of the different lines cannot be reproduced simultaneously (see Fig. 4). Indeed, when the excited transitions observed at 225 and 241 GHz with IRAM are reproduced, the fluxes of the CSO and HIFI lines are overproduced, in particular at 491, 600, 849, and 919 GHz (red dashed model in Fig. 4). On the contrary, if these latter lines are reproduced, the flux is underpredicted for the IRAM lines (green dotted model in Fig. 4). Although the choice of the velocity profiles can affect the line profiles, it is not possible to appreciably modify the intensities and decrease this disagreement.

To obtain an agreement for all the transitions, an increase of the jump temperature is necessary. Indeed, Fig. B4 shows that, with a jump temperature of 120 K, the model that reproduces the fluxes of the most excited HDO lines (226 and 242 GHz) is in better agreement with the fluxes of the lines at 491, 600, 849, and 919 GHz than the model with a jump at $T_j = 100 \text{ K}$. The fluxes of these four lines are, however, still overproduced. Consequently, we ran grid of models for higher jump temperatures (150, 180, 200, and 220 K) and compared the influence of the jump temperature on the line intensities. The best-fitting predictions obtained for $T_j = 150, 180, 200,$ and 220 K are shown in Figs B5, B6, 5, and B7, respectively. These four models reproduce relatively well the observations. The 491, 600, 849, and 919 GHz lines are quite sensitive to the jump temperature. Their intensities decrease with the increase of T_j . In

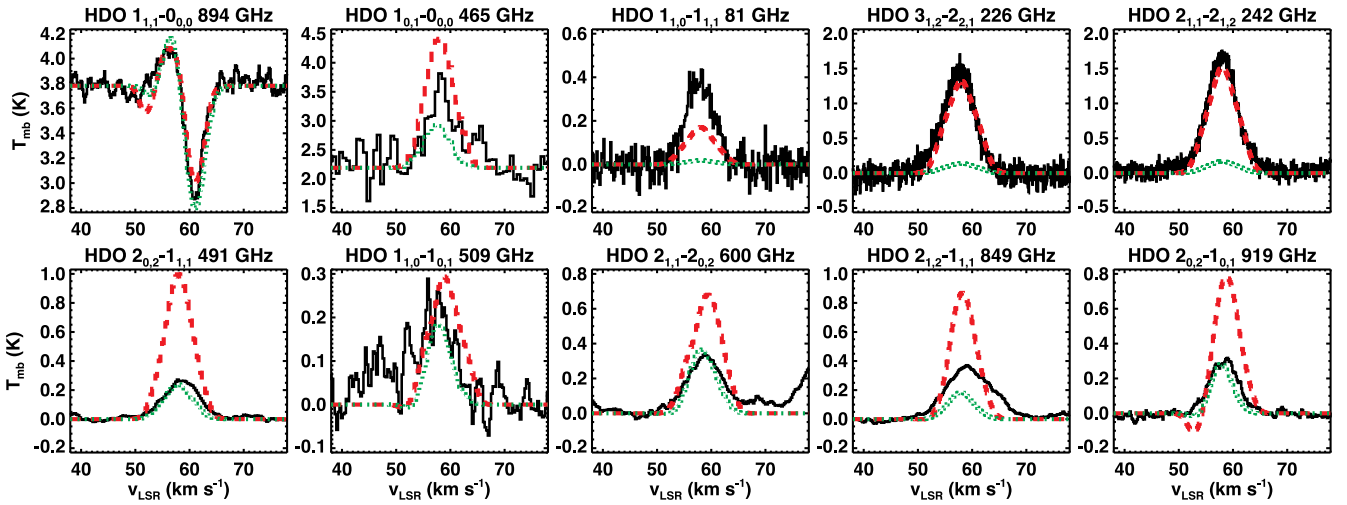


Figure 4. Black solid line: HDO lines observed with HIFI, IRAM, and CSO. Red dashed line: modelling for a jump temperature $T_j = 100$ K, an inner abundance $X_{in} = 3 \times 10^{-8}$, and an outer abundance $X_{out} = 8 \times 10^{-11}$. Green dotted line: modelling for a jump temperature $T_j = 100$ K, an inner abundance $X_{in} = 3 \times 10^{-9}$, and an outer abundance $X_{out} = 8 \times 10^{-11}$.

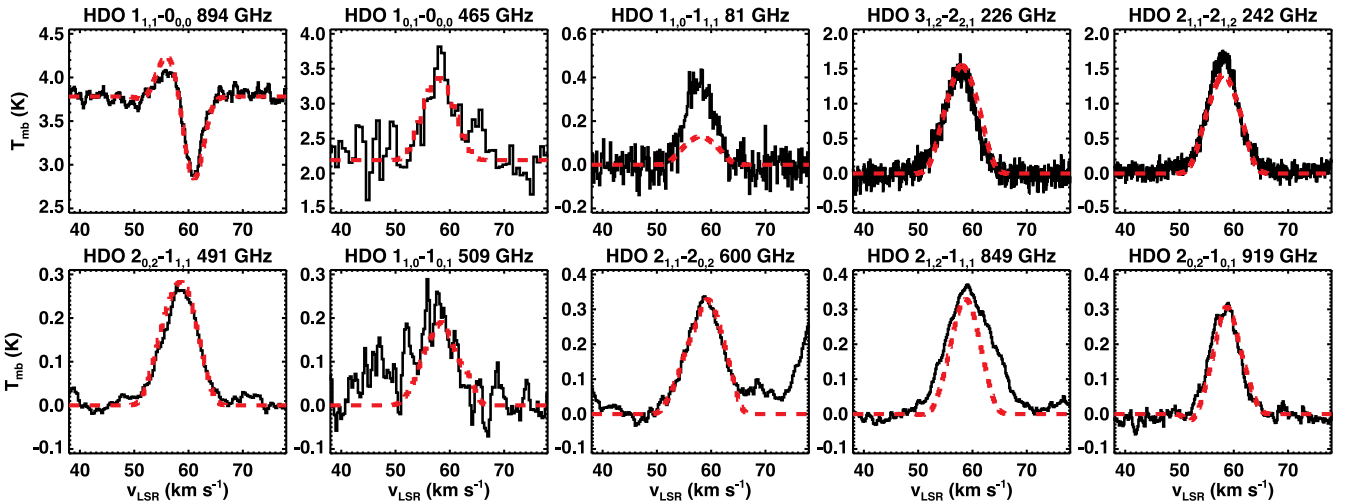


Figure 5. Black solid line: HDO lines observed with HIFI, IRAM, and CSO. Red dashed line: modelling for a jump temperature $T_j = 200$ K, an inner abundance $X_{in} = 2 \times 10^{-7}$, and an outer abundance $X_{out} = 8 \times 10^{-11}$.

Table 2. HDO and H₂O abundances obtained for different jump temperatures T_j .

T_j (K) ^a	θ (arcsec) ^a	$X_{in}(\text{HDO})$	$X_{out}(\text{HDO})$	$X_{in}(\text{H}_2^{18}\text{O})$	$X_{out}(\text{H}_2^{18}\text{O})$	$X_{in}(\text{H}_2\text{O})^b$	$X_{out}(\text{H}_2\text{O})^b$	$(\text{HDO}/\text{H}_2\text{O})_{in}^b$	$(\text{HDO}/\text{H}_2\text{O})_{out}^b$
100 ^c	4.5	–	–	–	–	–	–	–	–
120 ^c	3.5	–	–	–	–	–	–	–	–
150	2.5	1×10^{-7}	8×10^{-11}	4×10^{-7}	1.3×10^{-10}	1.6×10^{-4}	5.2×10^{-8}	6×10^{-4}	1.5×10^{-3}
180	1.9	1.5×10^{-7}	8×10^{-11}	7×10^{-7}	1.3×10^{-10}	2.8×10^{-4}	5.2×10^{-8}	5×10^{-4}	1.5×10^{-3}
200^d	1.7	2×10^{-7}	8×10^{-11}	9×10^{-7}	1.3×10^{-10}	3.6×10^{-4}	5.2×10^{-8}	6×10^{-4}	1.5×10^{-3}
220	1.5	3×10^{-7}	8×10^{-11}	1.2×10^{-6}	1.3×10^{-10}	4.8×10^{-4}	5.2×10^{-8}	6×10^{-4}	1.5×10^{-3}

Note: ^aSize of the region where the temperature is higher than T_j (diameter). It is derived from the structure determined by van der Tak et al. (2013).

^bAssuming $\text{H}_2^{16}\text{O}/\text{H}_2^{18}\text{O} = 400$.

^cFit is not good enough to determine the HDO abundances.

^dBest fit.

particular, for $T_j = 150$ and 180 K, their intensities are slightly overpredicted, while for $T_j \geq 220$ K, they start to be underpredicted. In view of these results, the best-fitting model is obtained for $T_j \sim 200$ K. Table 2 summarizes the HDO best-fitting abundances found for each jump temperature and the corresponding size of the jump abundance. The best fit was determined with a χ^2 min-

imization of the line profiles similar to what was done in Coutens et al. (2012), assuming a calibration uncertainty of 20 per cent for each line. As the HDO line at 849 GHz is probably blended with $^{13}\text{CH}_3\text{OH}$, we did not include it in the calculation. The reduced χ^2 obtained for the model with an abundance jump at 200 K is 1.3. The HDO inner abundance is strongly constrained by the high

number of emission lines used in the analysis. If we just consider the grid with $T_j = 200$ K, its value is between 1.7×10^{-7} and 2.1×10^{-7} . Consequently, the main uncertainty on the HDO inner abundance comes from the value assumed for the jump temperature ($\sim 1 \times 10^{-7}$ – 3×10^{-7} for $T_j \sim 150$ – 220 K). The outer abundance is mainly constrained by the absorbing component at 894 GHz and its uncertainty is found to be between 6×10^{-11} and 9×10^{-11} . The HDO $1_{1,0}$ – $1_{1,1}$ line at 81 GHz is not reproduced by any of the models within the 20 per cent calibration uncertainty and could maybe suffer of calibration problems at this low frequency with the IRAM 30-m telescope. Models with a two-jump abundance profile such as in Comito et al. (2010) were also attempted but do not improve the fit (see Appendix B3).

It clearly appears that, to reproduce the HDO line profiles, an increase of the jump temperature in the model is necessary. We cannot conclude, however, that the sublimation temperature for water ice is significantly higher than 100 K. Although some experiments actually favour an evaporation temperature of 110–120 K (Fraser et al. 2001), it is not sufficient to perfectly reproduce all the HDO transitions. The main reason for the modification of the jump temperature would be related to the size of the hot core, rather than to the water sublimation temperature itself. In this case, the size of the hot core in which the abundance of water increases after the evaporation of the icy mantles should be smaller (~ 2 arcsec instead of 4.5 arcsec), in order to lead to a better agreement between the model and the observations. This is also in agreement with the interferometric observations of the HDO lines at 225 and 241 GHz by Liu et al. (2013b) that are not spatially resolved with a beam size of 3.7×2.5 arcsec². Two explanations can be provided to explain the smaller size of the hot core. One would be that the physical structure derived by van der Tak et al. (2013) is unreliable at small scales. Indeed the structure determined here is only based on large-scale maps and the density profile is assumed to follow a power law. The density and temperature profiles could therefore be uncertain at small scales ($\theta \lesssim 5$ arcsec). In this case, the temperature actually would reach 100 K at a radius which is smaller than what the physical structure predicts (van der Tak et al. 2013). The second possible explanation is provided by the chemical models coupled with a dynamical approach, where the dynamical time-scales can be in competition with the chemical and adsorption/desorption time-scales. Indeed, as it can be seen e.g. in Aikawa et al. (2012) and Wakelam et al. (2014), the abundance increases gradually for a certain temperature range before a constant inner abundance is reached. The temperature where the inner abundance is constant is higher than 100 K but its exact value is dependent on the model parameters. It seems therefore possible that the constant inner abundance can be reached only at ~ 200 K. Some tests assuming a gradual abundance increase were attempted in Section 4.2.5 and this explanation seems to hold here.

4.2.3 Modelling of the H_2^{18}O lines with an abundance jump and estimate of the $\text{HDO}/\text{H}_2\text{O}$ ratios

A similar model with an abundance jump was carried out with the H_2^{18}O lines detected in this source to determine the $\text{HDO}/\text{H}_2\text{O}$ ratio throughout the envelope. The H_2^{16}O transitions detected with the HIFI instrument by Flagey et al. (2013) are not well suited to measure abundances, because of their large opacities. With its excitation level, the para- H_2^{18}O $3_{1,3}$ – $2_{2,0}$ transition observed at 203 GHz with the IRAM 30-m telescope is suitable to probe the hot core and derive the $\text{HDO}/\text{H}_2\text{O}$ ratio in the warm inner region. The H_2^{18}O fundamental lines previously detected with *Herschel*/HIFI by Flagey et al. (2013) are also used to constrain the $\text{HDO}/\text{H}_2\text{O}$ ratio in the envelope, as these lines combine both emission and absorption. Note that we only use here the ortho $1_{1,0}$ – $1_{0,1}$ transition at 548 GHz and the para $1_{1,1}$ – $0_{0,0}$ transition at 1102 GHz. The fundamental ortho $2_{1,2}$ – $1_{0,1}$ transition, which is observed at 1656 GHz in absorption, was not taken into account because of pointing problems affecting the observations. The source being fairly peaked on the continuum, an offset could lead to a significant loss of flux.

All the physical parameters are kept similar to those of the study of HDO. Figs B8, B9, 6, and B10 show the best-fitting models obtained for these three lines for the jump temperatures previously assumed for deuterated water, $T_j = 150, 180, 200,$ and 220 K, respectively. We assumed an ortho-to-para ratio of water equal to 3, corresponding to the thermal equilibrium value at high temperature (>50 K). This value is also consistent with the ratio determined in most of the foreground clouds on the line of sight towards bright continuum sources (Lis et al. 2010; Flagey et al. 2013). The best-fitting inner and outer H_2^{18}O abundances are summarized in Table 2. The reduced χ^2 is about 1.5 for the case $T_j = 200$ K. Assuming an observational uncertainty of 20 per cent for the excited para- H_2^{18}O line at 203 GHz, the inner abundance cannot be higher than 1.2×10^{-6} or lower than 7×10^{-7} for the model with $T_j = 200$ K. The outer abundance is estimated to be between 1.0×10^{-10} and 1.5×10^{-10} , based on an observational uncertainty of 20 per cent for the absorbing component of the para- H_2^{18}O transition at 1102 GHz. The H_2^{16}O abundances in Table 2 are estimated using an $\text{H}_2^{16}\text{O}/\text{H}_2^{18}\text{O}$ ratio of 400 (Wilson 1999).

The best-fitting $\text{HDO}/\text{H}_2\text{O}$ ratios are then equal to $\sim (5\text{--}6) \times 10^{-4}$ in the hot core and $\sim 1.5 \times 10^{-3}$ in the outer envelope. Even when considering the HDO and H_2^{18}O results with a 20 per cent calibration uncertainty, the outer $\text{HDO}/\text{H}_2\text{O}$ ratio (1.0×10^{-3} – 2.2×10^{-3}) is still higher than the inner $\text{HDO}/\text{H}_2\text{O}$ ratio (3.5×10^{-4} – 7.5×10^{-4} for $T_j = 200$ K). We ran models with a constant ortho/para H_2 ratio equal to 3 to check that the ortho/para H_2 ratio assumed in the model does not affect the results. The HDO and H_2^{18}O line profiles are exactly the same as with an LTE ortho/para ratio, confirming the variation of the $\text{HDO}/\text{H}_2\text{O}$ ratio from the cold to the warm regions.

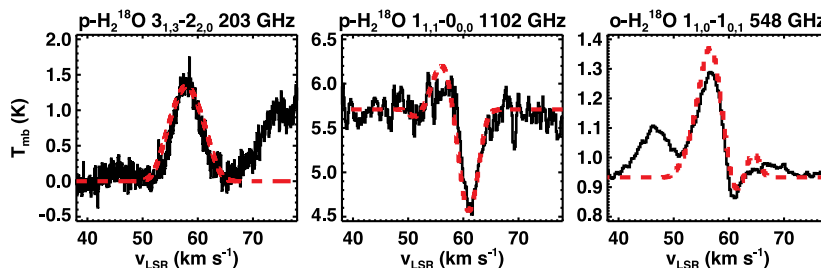


Figure 6. Black solid line: H_2^{18}O lines observed with HIFI and IRAM. Red dashed line: modelling for a jump temperature $T_j = 200$ K, an inner abundance $X_{\text{in}} = 9 \times 10^{-7}$, and an outer abundance $X_{\text{out}} = 1.3 \times 10^{-10}$.

4.2.4 Gradual decrease of the outer abundance from the cold to the warm regions

Although we used a constant abundance of HDO and H_2^{18}O in the cold envelope of G34, it is very probable that the water abundance shows variations in this region due to non-thermal desorption mechanisms. In particular, Mottram et al. (2013) showed that the desorption by the cosmic ray-induced UV field leads to an outer abundance of water decreasing gradually from the cold to the warm regions of low-mass protostars. To confirm that the presence of a gradual abundance decrease in the cold envelope does not affect the derived value of the HDO/ H_2O ratio in this region, we ran a modelling considering an equilibrium state between the desorption by the cosmic ray-induced UV field and the re-depletion on the grains. Using similar equations to those in Hollenbach et al. (2009) and Mottram et al. (2013), we get by equating desorption to depletion:

$$G_{\text{cr}} F_0 Y_x f_{s,x} n_{\text{gr}} \sigma_{\text{gr}} = n(x) n_{\text{gr}} \sigma_{\text{gr}} v_{\text{th},x}, \quad (4)$$

with F_0 the local interstellar flux of 6–13.6 eV photons assumed to be equal to 10^8 photons $\text{cm}^{-2} \text{s}^{-1}$, G_{cr} the scaling factor of the UV flux, Y_x the photodesorption yield for the molecule x ($\sim 10^{-3}$ for H_2O ; Öberg et al. 2009), $f_{s,x}$ the fraction of the molecule x on grains, n_{gr} the grain density, σ_{gr} the cross-sectional area of the grain, and $v_{\text{th},x}$ the thermal velocity. The thermal velocity is calculated according to the following formalism:

$$v_{\text{th},x} = \sqrt{\frac{8k_{\text{B}} T_{\text{k}}}{\pi m_x}}, \quad (5)$$

where k_{B} is the Boltzmann constant, T_{k} the gas temperature, and m_x the mass of the molecule x . The outer abundance of H_2O with respect to H_2 is then equal to

$$X_{\text{out}}(\text{H}_2\text{O}) = \frac{G_{\text{cr}} F_0 Y_{\text{H}_2\text{O}} f_{s,\text{H}_2\text{O}}}{v_{\text{th},\text{H}_2\text{O}} n_{\text{H}_2}}, \quad (6)$$

with n_{H_2} the H_2 density. Similarly we obtain for HDO:

$$X_{\text{out}}(\text{HDO}) = \frac{G_{\text{cr}} F_0 Y_{\text{HDO}} f_{s,\text{H}_2\text{O}}}{v_{\text{th},\text{HDO}} n_{\text{H}_2}} \left(\frac{\text{HDO}}{\text{H}_2\text{O}} \right), \quad (7)$$

and for H_2^{18}O :

$$X_{\text{out}}(\text{H}_2^{18}\text{O}) = \frac{G_{\text{cr}} F_0 Y_{\text{H}_2^{18}\text{O}} f_{s,\text{H}_2\text{O}}}{v_{\text{th},\text{H}_2^{18}\text{O}} n_{\text{H}_2}} \left(\frac{\text{H}_2^{18}\text{O}}{\text{H}_2\text{O}} \right). \quad (8)$$

The photodesorption yields for HDO and H_2^{18}O are assumed similar to those for H_2O (Öberg et al. 2009). The thermal velocity is approximatively the same due to their relatively similar masses. All the other parameters are independent of the molecules except the fraction $f_{s,x}$ of these molecules contained in the grain mantles which reflects the isotopic ratios, HDO/ H_2O and $\text{H}_2^{18}\text{O}/\text{H}_2^{16}\text{O}$, on the grains. The external UV field should also affect the external part of the outer envelope. But, due to the very small constraints on these different mechanisms, we only considered the desorption by the cosmic ray-induced UV field.

We ran a grid of models for the case $T_{\text{j}} = 200$ K, keeping the inner abundances determined previously ($X_{\text{in}}(\text{HDO}) = 2 \times 10^{-7}$ and $X_{\text{in}}(\text{H}_2^{18}\text{O}) = 9 \times 10^{-7}$). Different values were then assumed for the factors $W_{\text{HDO}} = G_{\text{cr}} f_{s,\text{H}_2\text{O}} \text{HDO}/\text{H}_2\text{O}$ and $W_{\text{H}_2^{18}\text{O}} = G_{\text{cr}} f_{s,\text{H}_2\text{O}} \text{H}_2^{18}\text{O}/\text{H}_2^{16}\text{O}$. Assuming $\text{H}_2^{18}\text{O}/\text{H}_2^{16}\text{O} = 400$ (Wilson 1999) and $f_{s,\text{H}_2\text{O}} = 1$ (the icy grain mantles are constituted entirely of H_2O), the best-fitting model of the H_2^{18}O lines gives a scaling factor G_{cr} of about 1.6×10^{-3} . If water represents only 50 per cent of the grain mantles, G_{cr} is then equal to 3.2×10^{-3} leading to a cosmic ray-induced UV field of $\sim 3 \times 10^5$ photons $\text{cm}^{-2} \text{s}^{-1}$.

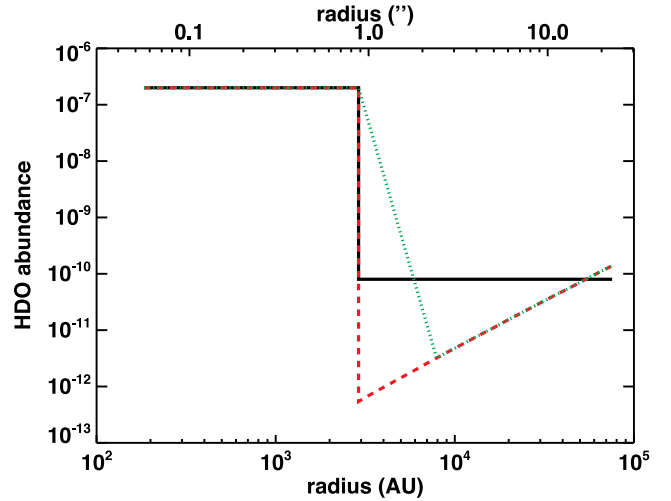


Figure 7. Best-fitting abundance profiles obtained for HDO when the outer abundance (region at $T < 200$ K) is constant (black solid line, Section 4.2.2), when it decreases from the cold regions to the region at $T = 200$ K (red dashed line, Section 4.2.4), and when it decreases from the cold regions to the region at $T = 100$ K and increases from $T = 100$ to 200 K (green dotted line, see Section 4.2.5). The temperature reaches 200 K at a radius of 2700 au (~ 0.9 arcsec, see Fig. B1).

These values represent, however, only upper limits, since the desorption by the external UV field is not taken into account in the analysis. The typical value of the cosmic ray-induced UV flux ($G_{\text{cr}} \sim 10^{-4}$; e.g. Prasad & Tarafdar 1983; Shen et al. 2004) is then consistent with the upper limit derived here ($G_{\text{cr}} \lesssim 3 \times 10^{-3}$).

The best-fitting abundance profile determined for HDO when the outer abundance decreases from the cold to the warm regions is presented in Fig. 7 (red dashed line). The HDO/ H_2O ratio in the outer envelope is equal to 1.3×10^{-3} . It is then, once again, higher than in the hot core ($\sim (5-6) \times 10^{-4}$). The HDO and H_2^{18}O line profiles predicted with the RATRAN code (see red dashed lines in Figs 8 and 9) are relatively similar to those in Figs 5 and 6 that assume a two-step abundance profile with a jump at 200 K. The fit is even better for the H_2^{18}O and HDO fundamental transitions (HDO: 894 GHz; H_2^{18}O : 548 and 1102 GHz), as the predicted intensity of their emission is now in agreement with the observations. Some of the HDO lines (509, 600, and 919 GHz) show small self-absorptions on their blueshifted side. However, these defects could probably disappear with slightly different velocity profiles. Indeed, the velocity profiles used here were only adapted for the models with the abundance jumps (see Appendix B2).

4.2.5 Gradual increase of the water abundance profile at the cold envelope/hot core transition

In Section 4.2.2, we mentioned that a model with a gradual increase of the HDO abundance at the cold envelope/hot core transition could potentially explain why we need a higher jump temperature than 100 K to reproduce the HDO line profiles. Here we show the results obtained with both a decrease of the outer abundance from the outermost regions to the regions at 100 K and a gradual increase from 100 to 200 K. This type of profile is then relatively similar to the predictions of chemical models coupled with a dynamical approach (Aikawa et al. 2012; Wakelam et al. 2014). The HDO inner abundance is equal to 2×10^{-7} and the outer abundance follows the trend described in Section 4.2.4. The abundance profile used and

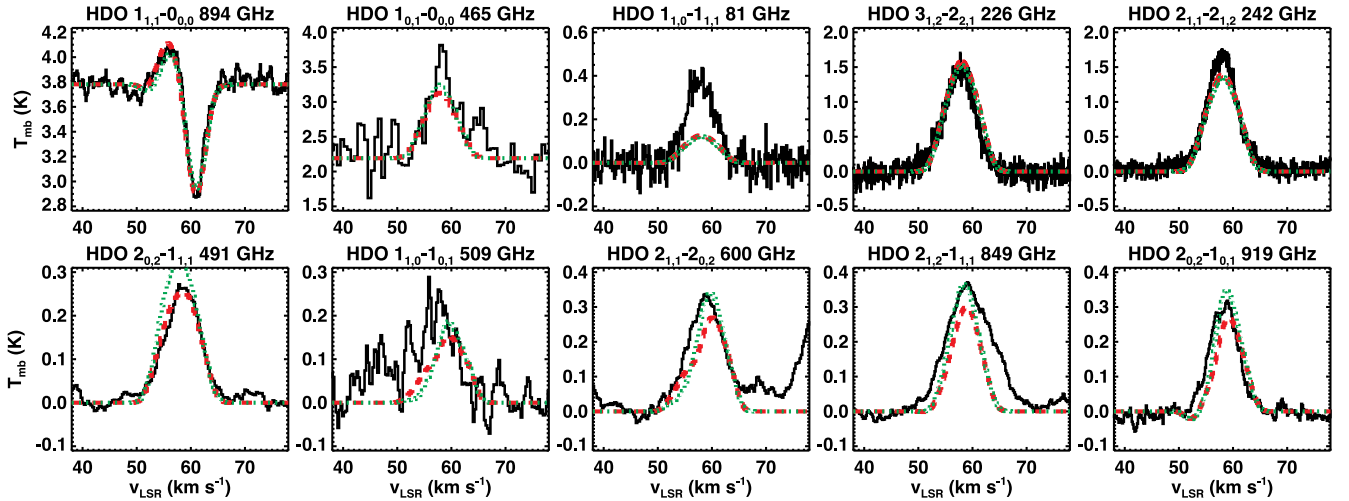


Figure 8. Black solid line: HDO lines observed with HIFI, IRAM, and CSO. Red dashed line: modelling for a constant inner abundance $X_{\text{in}} = 2 \times 10^{-7}$ ($T \geq 200$ K) and an outer abundance ($T < 200$ K) decreasing from the cold to the warm regions (see Section 4.2.4). Green dotted line: modelling for a constant inner abundance $X_{\text{in}} = 2 \times 10^{-7}$ ($T \geq 200$ K), an abundance gradually increasing from 100 to 200 K, and an outer abundance ($T < 100$ K) decreasing from the cold to the warm regions (see Section 4.2.5).

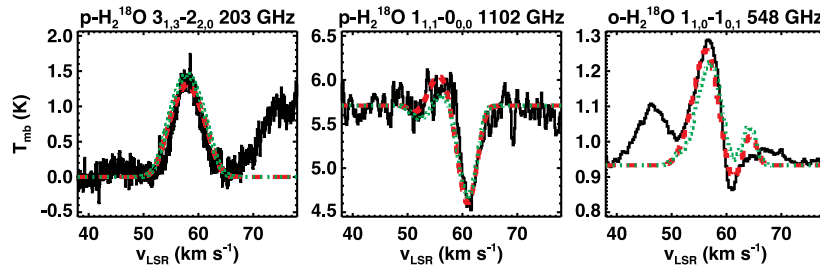


Figure 9. Black solid line: H_2^{18}O lines observed with HIFI and IRAM. Red dashed line: modelling for a constant inner abundance $X_{\text{in}} = 9 \times 10^{-7}$ ($T \geq 200$ K) and an outer abundance ($T < 200$ K) decreasing from the cold to the warm regions (see Section 4.2.4). Green dotted line: modelling for a constant inner abundance $X_{\text{in}} = 9 \times 10^{-7}$ ($T \geq 200$ K), an abundance gradually increasing from 100 to 200 K, and an outer abundance ($T < 100$ K) decreasing from the cold to the warm regions (see Section 4.2.5).

the result of the model for HDO are shown in Figs 7 and 8 (green dotted line), respectively. This model also appears very similar to the model with an abundance jump at 200 K (see Fig. 5). A model with both an abundance decrease (with temperature) in the colder envelope and an increase of the abundance towards the hot core is probably more realistic than the jump abundance assumption and could explain why the hot core is smaller than expected. It is, however, important to note that the temperature range of the gradual abundance increase is not known. We assume here the range 100–200 K but it could be slightly different and a specific range is probably dependent on the dynamics. The result of this modelling should thus be considered only qualitatively. We can however conclude that this type of abundance profile allows us to reproduce the HDO line profiles as well as the abundance jump models at ~ 150 –220 K.

We ran a similar model for the H_2^{18}O lines. The model (presented in Section 4.2.5) with a gradual increase of the abundance at the cold envelope/hot core transition is presented in Fig. 9 (green dashed lines). The lines are here again reproduced as well as by the jump abundance models. The HDO/ H_2O ratio shows consequently the same variation between the inner and outer regions as found before, i.e. 5.6×10^{-4} at $T > 200$ K and 1.3×10^{-3} at $T < 100$ K.

4.3 Comparison with previous studies

The singly deuterated form of water has been studied towards many high-mass hot cores with ground-based telescopes (Jacq et al. 1990; Gensheimer et al. 1996; Pardo et al. 2001; van der Tak et al. 2006). These studies are relevant for the hot core study but do not directly address for the cold external envelope, since the observations of the ground HDO transition at 894 GHz with a very good signal-to-noise ratio are necessary in order to disentangle the contribution from the hot core to the contribution of the cold envelope. The launch of the *Herschel Space Observatory* dramatically changed the situation, with the access to the high frequency range with many HDO transitions available in addition to the ground-state transition. The D/H ratio in water remained for a long time very poorly known since the study of water was based on observations suffering from dilution in the large beams of the *ISO*, *SWAS* and the *Odin* satellite as well as from large opacities. The only way to study water from the ground was to use the H_2^{18}O transition available with some telescopes at 203 GHz (Jacq et al. 1988; van der Tak et al. 2006; Jørgensen & van Dishoeck 2010; Persson, Jørgensen & van Dishoeck 2012; Persson et al. 2013). With the help of this line, the water deuterium fractionation was previously estimated in the high-mass star-forming region G34 by Jacq et al.

(1990), Gensheimer et al. (1996), and Liu et al. (2013b). They found, in its hot core, HDO/H₂O ratios ranging between 1×10^{-4} and 4×10^{-4} . Since our modelling in the hot core region is mostly dominated by the 81, 226, and 241 GHz transitions accessible from the ground, these values are relatively consistent with our estimate of $(5\text{--}6) \times 10^{-4}$ both with the rotational diagram approach and the non-LTE 1D analysis. Note that we assumed an H₂¹⁶O/H₂¹⁸O ratio of 400, whereas the previous studies assumed 500. In addition, the HDO/H₂O ratio found in this hot core is consistent with the average HDO/H₂O ratio (a few 10^{-4}) found in other high-mass sources (Jacq et al. 1990; Gensheimer et al. 1996; Pardo et al. 2001; van der Tak et al. 2006; Emprechtinger et al. 2013).

In the hot core, we also determined the water abundance (relative to H₂) to be a few $\times 10^{-4}$. Similar values were estimated in other high-mass hot cores (Chavarría et al. 2010; Herpin et al. 2012; Neill et al. 2013), although lower values were also found, for example, in NGC 6334 I ($\sim 10^{-6}$; Emprechtinger et al. 2013). The value of 10^{-4} is comparable to the observed abundance of solid water and together with the derived HDO/H₂O abundance ratios of 10^{-4} – 10^{-3} suggests that the origin of the observed water is evaporation of grain mantles.

Recently, Liu et al. (2013b) also attempted to constrain the D/H ratio for water in the outer envelope of G34 using the 894 GHz transition observed from the ground with the Atacama Pathfinder Experiment (APEX). From a RATRAN modelling using an abundance jump profile at 100 K, they failed to reproduce the profile of this ground state transition leading to a very uncertain value for the D/H ratio in the outer region of the envelope of $(1.9\text{--}4.9) \times 10^{-4}$. With the sensitivity of *Herschel*/HIFI observations of the 894 GHz transition, it became possible to measure accurately the D/H ratio of water in low- (Coutens et al. 2012, 2013b) and high-mass protostars, from the hot core region to the cold external envelope. We showed here that, with a value of $(1.0\text{--}2.2) \times 10^{-3}$ in the colder envelope, the HDO/H₂O ratio is indeed higher than the estimate by Liu et al. (2013b). It is also higher than in the hot core. A similar behaviour was discovered in the low-mass sources IRAS 16293 and NGC 1333 IRAS 4A (Coutens et al. 2013a,b). But this is the first time that a radial variation of the D/H ratio has been observed towards a high-mass star-forming region. The HDO/H₂O ratio derived in the colder envelope of G34 is among the highest values found in high-mass sources. It is close to the high value of $(2\text{--}4) \times 10^{-3}$ found in Orion KL (Persson et al. 2007; Neill et al. 2013) but lower by more than a factor of 10 than in the absorbing layer of low-mass protostars (Coutens et al. 2012, 2013b).

5 CHEMICAL MODELLING

In order to study the chemical pathways that could lead to the observed HDO and H₂O abundances and their corresponding ratio, we modelled the chemical evolution of the source as a function of its radius, using the full gas–grain chemical model NAUTILUS (Hersant et al. 2009).

5.1 Model

NAUTILUS is a gas–grain chemical code adapted from the original code developed by the Herbst group (Hasegawa & Herbst 1993). It solves the kinetic equations of gas phase chemistry, takes into account grain surface chemistry, and interactions between both phases (adsorption, thermal, and non-thermal desorption). The rate equations follow Hasegawa, Herbst & Leung (1992) and Caselli, Hasegawa & Herbst (1998). More details on the processes included

in the code are presented by Semenov et al. (2010). The chemical network is adapted from Aikawa et al. (2012) and Furuya et al. (2012). As pointed out by Pagani, Salez & Wannier (1992), Flower, Pineau des Forêts & Walmsley (2004, 2006a,b), Walmsley, Flower & Pineau des Forêts (2004), and Pagani et al. (2009), considering ortho and para spin modifications of various H and D bearing species is important due to some reactions which are much faster with ortho-H₂ than para-H₂, and can change the entire chemistry of deuterium fractionation. Thus, we extended the network including the ortho, para, and meta states of H₂, D₂, H₃⁺, H₂D⁺, D₂H⁺, and D₃⁺. For the reactions involving these species, we have applied spin selection rules to know which reactions are allowed, and have determined branching ratios assuming a total scrambling and a pure nuclear spin statistical weight. Some of the rate coefficients of these reactions have been theoretically or experimentally determined (Marquette, Rebrion & Rowe 1988; Jensen et al. 2000; McCall et al. 2004; Dos Santos, Kokouline & Greene 2007; Hugo, Asvany & Schlemmer 2009; Honvault et al. 2011a, 2011b; Dislaire et al. 2012) and for these we used the calculated or measured values. We have benchmarked our model against some previous work that includes spin-state chemistry, using the same conditions as described in fig. 8 of Pagani et al. (2009) and fig. 4 of Sipilä, Caselli & Harju (2013): a temperature of ~ 10 K and a density from $\sim 10^5$ to $\sim 10^6$ cm⁻³. Minor differences in abundances do exist, since the networks, the models, and the input parameters can be slightly different, but the result is globally similar. A notable difference is however seen for HD after 10^5 yr as compared with Sipilä et al. (2013). They predict a decrease of its gas phase abundance by one order of magnitude at 10^6 yr. Under the same conditions, we predict a decrease in the gas phase HD abundance of only a factor of ≈ 2 , similar to the model of Albertsson et al. (2013, 2014, private communication). The inclusion in our model of photodesorption and reactive desorption may have some effect on HD depletion. Photodesorption due to direct interstellar UV photons and secondary photons generated by cosmic rays, as well as the exothermic association between the surface species H and D, may both release enough HD molecules to the gas phase to lower the HD depletion. The network and a benchmark will be presented in more detail in a forthcoming paper (Hincelin et al., in preparation).

In our model, elemental and initial abundances follow Hincelin et al. (2011). Initially, the ortho-to-para H₂ ratio is set to its statistical value of 3, and deuterium is assumed to be entirely in HD form with an abundance of 1.5×10^{-5} relative to total hydrogen, following Kong et al. (2013). Note that the time-scale for conversion to a thermal ortho-to-para H₂ ratio is a few times 10^5 to a few times 10^6 yr at 10 K depending on the density, as in Pagani et al. (2009). In the evolutionary sequence of high-mass star formation proposed by Beuther et al. (2007) and Zinnecker & Yorke (2007), infrared dark clouds (IRDCs) are expected to be the first stage. Comparing observations of high-mass star-forming regions with advanced gas–grain chemical modelling, Gerner et al. (2014) derived a chemical age for this stage of around 10^4 yr. The mean density and temperature of IRDCs are, respectively, 10^5 cm⁻³ and 16 K (Sridharan et al. 2005). From the initial elemental and chemical abundances, we have computed the chemical evolution over a period of 10^4 yr, corresponding to t_{IRDC} in Fig. 10, with a temperature of 16 K, a proton density of 2×10^5 cm⁻³, and a visual extinction of 30. In our standard model, we use a cosmic ray ionization rate of 1.3×10^{-17} s⁻¹, but also use a value 10 times higher, as discussed in Section 5.2. Following this first phase, we switched to a time-independent one-dimensional physical structure of G34 derived by van der Tak et al. (2013) as seen in Fig. B1, and allowed the time-dependent chemistry to

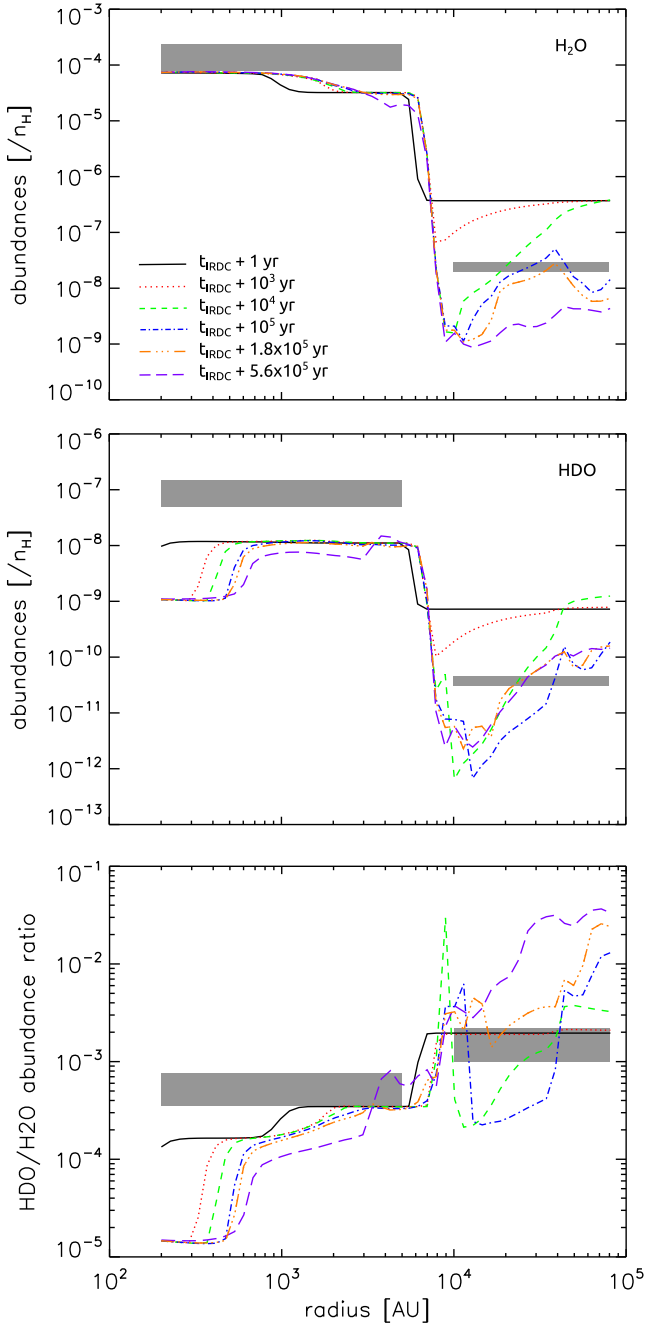


Figure 10. Top and centre: calculated gas phase abundances of H_2O and HDO relative to the total density of protons. Grey areas show observational values and uncertainties of H_2O and HDO , observed in the hot inner core and the colder envelope. Bottom: $\text{HDO}/\text{H}_2\text{O}$ gas phase abundance ratio. Grey areas show observational values and uncertainties of $\text{HDO}/\text{H}_2\text{O}$ gas phase abundance ratio observed in the hot inner core and the colder envelope (see Sections 4.2.2 and 4.2.3 for information about uncertainties). Both abundances are plotted as a function of the radius of the source. The results are time dependent, and the colours and types of lines correspond to different values after the first initial phase: black solid lines ($t = t_{\text{IRDC}} + 1$ yr), red dotted lines ($t = t_{\text{IRDC}} + 10^3$ yr), green short dashed lines ($t = t_{\text{IRDC}} + 10^4$ yr), blue dashed-dotted (one dot) lines ($t = t_{\text{IRDC}} + 10^5$ yr), orange dashed-dotted (three dots) lines ($t = t_{\text{IRDC}} + 1.8 \times 10^5$ yr), and purple long dashed lines ($t = t_{\text{IRDC}} + 5.6 \times 10^5$ yr).

continue to evolve independently at each value of the radius of the source.

5.2 Results

Fig. 10 shows the computed fractional abundances for gaseous HDO and H_2O relative to the total proton density and their ratio as a function of the radius of the source, at different times following the IRDC stage. The computed values can be compared with the values that best fit the observations, as listed in Table 2. The observational values are given for two points in the table, the inner hot core and the colder envelope, but these values are represented as areas in the figures with their height referring to uncertainty and their length to the length of the inner and outer regions. Note that observational results may not be constant as a function of radius, as shown for the abundances in Sections 4.2.4 and 4.2.5.

During the IRDC phase, water, and HDO are present mainly on the grain surfaces, with the water abundance $\approx 10^{-4}$. Once we apply the physical profile of the source, the temperature in the inner region, greater than ~ 100 K, is high enough to allow the rapid desorption of H_2O and HDO , and a transition region is observed around 6×10^3 au, which corresponds to ~ 100 K. Beyond 6×10^3 au, the reverse effect is observed: molecules are slowly adsorbed on to grain surfaces depending on the radius, because the density of the source is now higher than during the IRDC phase. The rate of adsorption is directly proportional to the density, and since the density is higher for small radii, the gaseous molecules are adsorbed more quickly closer to the transition region. This effect is clearly seen at times of 10^3 yr and longer. While the gas phase water fractional abundance predicted by the chemical model in the inner core (radius ≤ 5000 au) is almost constant, at 10^{-4} – 10^{-5} relative to the total proton density, in the colder envelope, the water abundances lie between a few $\times 10^{-7}$ and 10^{-9} depending on the radius and the time. This dependence also holds for HDO , which possesses an inner core abundance between 10^{-8} and 10^{-9} , and an outer abundance between a few $\times 10^{-9}$ and 10^{-12} .

In addition to these gas–grain interactions, chemical reactions are also occurring. In the inner core, gaseous water is mainly destroyed by reactions with atomic hydrogen: $\text{H} + \text{H}_2\text{O} \rightarrow \text{OH} + \text{ortho-H}_2$, and $\text{H} + \text{H}_2\text{O} \rightarrow \text{OH} + \text{para-H}_2$. However, water is efficiently reformed by the reverse reactions, so its abundance does not change significantly. In the same region, HDO is also mainly destroyed by reactions with atomic hydrogen: $\text{H} + \text{HDO} \rightarrow \text{OH} + \text{HD}$, $\text{H} + \text{HDO} \rightarrow \text{OD} + \text{ortho-H}_2$, and $\text{H} + \text{HDO} \rightarrow \text{OD} + \text{para-H}_2$. Although HDO is also reformed by the reverse reactions, these processes are sufficiently slower than the destruction reactions that the HDO abundance decreases, with an efficiency depending on the local temperature. This is indicated by the lines in the centre panel of Fig. 10, particularly within a radius of 1000 au. Thus, we observe a general decrease of the $\text{HDO}/\text{H}_2\text{O}$ ratio in the hot inner core as a function of time.

In the colder envelope, at larger radii, the H_2O gas phase abundance is reduced due to adsorption, as discussed above, and ion–molecule reactions, particularly the reaction with HCO^+ , which forms H_3O^+ and CO . Before $t = t_{\text{IRDC}} + 10^4$ yr, HCO^+ mainly reacts with carbon atoms, and after this time, the carbon atom abundance is low enough to allow an increase of the HCO^+ abundance through ion–molecule reactions involving CO . Although HDO also reacts with HCO^+ , it is partially reformed by ion–molecule reactions involving H_2DO^+ , and dissociative recombination of H_2DO^+ with an electron. H_2O is also reformed by reactions involving H_3O^+ , but not as efficiently as HDO . At later times, the

abundances of HDO^+ and H_2DO^+ are increased, while the ones of H_2O^+ and H_3O^+ are decreased, so that the $\text{HDO}/\text{H}_2\text{O}$ abundance ratio increases.

At 10^4 au, next to the transition region, the temperature and density are, respectively, equal to 80 K and 10^6 cm^{-3} . Here, there is a complex competition between the formation of HDO and H_2O in the gas phase and the adsorption and desorption of these molecules. For this reason, we get temporarily a peak in the $\text{HDO}/\text{H}_2\text{O}$ ratio around 10^4 and 10^5 yr (respectively the green and blue peak). The main gas phase reactions involved are the following: H_3O^+ and H_2DO^+ react with DCN, DNC, HCN, and HNC, which form HDO and H_2O . Besides, after 10^4 yr, H_2CO plays also a role: it is slowly released from the grain surface, and reacts efficiently with OH and OD to form, respectively, H_2O and HDO. However, at this temperature and density, adsorption of HDO and H_2O is still quite efficient, and removes a part of these molecules from the gas phase.

If we compare the computed abundances of water and HDO with the observational values, seen as grey areas in Fig. 10, the H_2O abundances are in good agreement in both the hot inner core and the colder outer envelope. This also holds true for HDO in the colder envelope; however, our model does not produce enough HDO in the hot inner core at all times. Specifically, our values are 5–50 times less than those indicated by the observations, depending on the time and the radius. Given the low abundance of HDO in the hot inner core, our calculated gaseous $\text{HDO}/\text{H}_2\text{O}$ ratio is lower than the observed one throughout this region, while in the colder outer envelope, our ratio lies within the range of the observational values at selected times. Note that the observational abundances and ratio may not be constant as a function of radius in the two regions, so more constraints are necessary to compare with the model results.

The HDO abundance profiles in the cold outer region from Fig. 10 favour the best-fitting abundance profile for water from Fig. 7, which increases with radius in the cold envelope. A comparison between the HDO profiles of these two figures leads to the best agreement around $t = t_{\text{IRDC}} + 10^5$ yr. This time corresponds to the best-fitting chemical age of Germer et al. (2014): their high-mass protostellar object stage, the stage just after the IRDC stage, lasts $\sim 6 \times 10^4$ yr, and the following stage, the hot molecular core stage, lasts $\sim 4 \times 10^4$ yr, which give a total similar to ours.

We have tested the sensitivity of H_2O and HDO to the cosmic ray ionization rate, using a value of $1.3 \times 10^{-16} \text{ s}^{-1}$, which is 10 times higher than the standard rate. This value is close to the upper limit derived in this source (see Section 4.2.4). Cosmic rays are the main source of ions in clouds, and formation and destruction of neutral species involve mainly reactions with charged species. As a consequence, most of the molecules are sensitive to the cosmic ray ionization rate (Wakelam et al. 2010). Compared with our standard model, in the cold envelope, the gas phase H_2O abundance is decreased by one order of magnitude at early times after the IRDC phase. Then, H_2O is reformed quite efficiently so that the final abundance is one order of magnitude higher than with our standard model. In the same region, the HDO abundance is increased by a factor of 10–100 depending on the time. The $\text{HDO}/\text{H}_2\text{O}$ ratio is then enhanced, and higher than the observational value by a factor of ~ 100 and < 2 , respectively, at early and later times. In the inner core, the H_2O abundance is slightly increased to a value $\geq 10^{-4}$ at all times. The HDO abundance is more sensitive at early times to the cosmic ionization rate: it is first increased by a factor of 100, but then the value tends to decrease to the same one as in our standard model. The $\text{HDO}/\text{H}_2\text{O}$ ratio is also enhanced, up to a factor of 100

at early times, but tends to decrease to the same value as in our standard model. In the IRDC phase and the cold envelope, gaseous H_2O is mainly formed by reactions involving H_3O^+ and destroyed by reactions with HCO^+ and C^+ , while H_2DO^+ is the main reactant involved in the formation of HDO. In the inner hot core, the abundances of H_2O and HDO are mainly changed due to OH and OD which are sensitive to the cosmic ray ionization rate (Wakelam et al. 2010).

We have also tested the sensitivity of our modelling to the inclusion of spin-state chemistry, and provide in Appendix C the results of a simulation using our chemical network without considering the spin states. Our main conclusion is that the gas phase HDO abundance is not only sensitive to the inclusion of spin-state chemistry at low temperature, but also at high temperature, although the difference is less strong. In addition, the H_2O abundance is slightly sensitive at longer times to the spin-state chemistry in the cold envelope region, but not in the hot inner core region. The overall ratio $\text{HDO}/\text{H}_2\text{O}$ decreases if we take into account spin-state chemistry, as it can be predicted based simply on the thermodynamics of protonated ion–HD exchange reactions.

5.3 Comparison with other studies

Below we compare our results for water and HDO both in the gas and on ice mantles with those of earlier studies. We first consider ice mantles. Some of these studies include spin-state chemistry while others do not.

Several groups theoretically studied deuteration of water in star-forming regions (i.e. Cazaux, Caselli & Spaans 2011; Aikawa et al. 2012; Sipilä et al. 2013; Taquet et al. 2013; Taquet, Charnley & Sipilä 2014). These studies focus on low-mass star formation regions or cold conditions, and as a consequence generally deal with lower temperatures and densities than ours. However, considering the external region of the cold envelope of our source, where the conditions are the closest to these studies (30 K and 10^5 cm^{-3}), it is worth making some comparisons with our ice results. Our $\text{HDO}/\text{H}_2\text{O}$ ice ratio in the cold envelope varies between 10^{-4} and 10^{-3} depending on the time. The larger the time, the larger the ratio. We can compare our values to those in figs 11 and 12 in Sipilä et al. (2013) and fig. 8 in Taquet et al. (2013). These studies also include spin-state chemistry. In general, we predict a lower $\text{HDO}/\text{H}_2\text{O}$ ice ratio than these studies. Despite our slightly higher temperature, and multiple differences between our models, the initial ortho-to-para H_2 ratio may be the main reason, since a higher value tends to decrease the deuterium fractionation. Cazaux et al. (2011) and Aikawa et al. (2012), who did not consider the spin-state chemistry, predicted an $\text{HDO}/\text{H}_2\text{O}$ ice ratio of ~ 0.01 , which then can be considered as an upper limit.

Aikawa et al. (2012) and Taquet et al. (2014) studied the deuteration of molecules as a function of the radius of a forming protostellar core. Here we can compare calculated $\text{HDO}/\text{H}_2\text{O}$ ratios in the gas phase. Their temperature and density gradient along the radius is quite important, from ~ 10 K and $\sim 10^4 \text{ cm}^{-3}$ to several hundred Kelvin and 10^{12} cm^{-3} , close to the range of conditions of our source. Note that these studies include a dynamical physical structure instead of a static structure. Despite the differences between our model and these earlier studies, we obtain the same qualitative pattern, in which the gas phase water abundance is higher in the inner and hot region, while it is lower in the outer and cold region. In the outer region, the abundance is governed mainly by the density, and as a consequence, tends to be lower when the density gets higher.

Their HDO/H₂O ratio changes by one to two orders of magnitude between the cold region and the hot region, and is higher in the colder region.

6 CONCLUSIONS

10 lines of HDO and three lines of H₂¹⁸O covering a broad range of upper energy levels (22–204 K) were detected with the *Herschel*/HIFI instrument, the IRAM 30-m telescope, and the CSO towards the high-mass star-forming region G34. Using a 1D non-LTE radiative transfer code, we constrained the abundance distribution of HDO and H₂¹⁸O throughout the envelope from the hot core to the colder regions. To reproduce the HDO line profiles, it is necessary to assume an abundance jump at a temperature higher than 100 K (~150–220 K), which suggests that the hot core is smaller than expected. This could be explained by the fact that the water abundance increases gradually within a certain temperature range between the cold envelope and the hot core, as suggested by some chemical models considering dynamics (Aikawa et al. 2012; Wakelam et al. 2014). Another explanation would be that the structure is relatively uncertain at small scales. Similar studies (including observations of the HDO lines at 226 and 242 GHz, as well as some HIFI lines at 491, 600, or 919 GHz) should be carried out towards other high-mass sources to know if this higher jump temperature is specific to G34 or common to other objects. Using different types of water abundance profiles, we showed that the water deuterium fractionation in the hot core and in the colder envelope is strongly constrained. Assuming calibration uncertainties of 20 per cent, the HDO/H₂O ratio is estimated to be about $(3.5\text{--}7.5) \times 10^{-4}$ in the hot core. It is in agreement with the value derived with the rotational diagram analysis of the IRAM 30-m lines as well as with previous studies (Jacq et al. 1990; Liu et al. 2013b). In the colder gas, we determined the HDO/H₂O ratio to be about $(1.0\text{--}2.2) \times 10^{-3}$, including the uncertainties. Although radial variations of the water deuterium fractionation have already been observed in low-mass protostars (Coutens et al. 2012, 2013a,b), this is the first time that a decrease of the water deuterium fractionation in the warmer regions has been measured in a high-mass star-forming region. Finally, we modelled the chemical evolution of G34 as a function of its radius and showed that our model reproduces relatively well the observational results that assumed an increase of the water abundance with radius in the cold regions (see Figs 7 and 10). The comparison of the chemical model and the observations favours an age of 10⁵ yr after the IRDC stage, which is consistent with the age derived for hot molecular cores by Gerner et al. (2014).

ACKNOWLEDGEMENTS

The authors are grateful to the anonymous referee for useful and pertinent comments and suggestions. They thank K. Furuya and Y. Aikawa for providing the initial chemical network of deuterated species and N. Flagey for providing the reduced HIFI data of H₂¹⁸O. They would also like to thank M. Hajigholi for fruitful discussions regarding the source modelling. AC and CV thank PCMI for support of the *Herschel* HIFI project on deuterated water. CMP acknowledges generous support from the Swedish National Space Board. Support for this work was also provided by NASA through an award issued by JPL/Caltech.

This work is based on observations carried out with the HIFI instrument onboard the *Herschel Space Observatory*, the Institut de RadioAstronomie Millimétrique (IRAM) 30-m Telescope, and

the Caltech Submillimeter Telescope (CSO). *Herschel* is an ESA space observatory with science instruments provided by European-led principal investigator consortia and with important participation from NASA. HIFI has been designed and built by a consortium of institutes and university departments from across Europe, Canada, and the USA under the leadership of SRON Netherlands Institute for Space Research, Groningen, The Netherlands and with major contributions from Germany, France, and the USA. Consortium members are: Canada: CSA, U. Waterloo; France: IRAP (formerly CESR), LAB, LERMA, IRAM; Germany: KOSMA, MPIfR, MPS; Ireland: NUI Maynooth; Italy: ASI, IFSI-INAF, Osservatorio Astrofisico di Arcetri-INAF; Netherlands: SRON, TUD; Poland: CAMK, CBK; Spain: Observatorio Astronómico Nacional (IGN), Centro de Astrobiología (CSIC-INTA); Sweden: Chalmers University of Technology – MC2, RSS and GARD, Onsala Space Observatory, Swedish National Space Board, Stockholm University – Stockholm Observatory; Switzerland: ETH Zurich, FHNW; USA: Caltech, JPL, NHSC. IRAM is supported by INSU/CNRS (France), MPG (Germany), and IGN (Spain). The CSO is operated by the California Institute of Technology under cooperative agreement with the National Science Foundation (AST-0838261).

REFERENCES

- Aikawa Y., Wakelam V., Hersant F., Garrod R. T., Herbst E., 2012, *ApJ*, 760, 40
- Albertsson T., Semenov D. A., Vasyunin A. I., Henning T., Herbst E., 2013, *ApJS*, 207, 27
- Albertsson T., Indriolo N., Kreckel H., Semenov D., Crabtree K. N., Henning T., 2014, *ApJ*, 787, 44
- Alexander C. M. O. D., Bowden R., Fogel M. L., Howard K. T., Herd C. D. K., Nittler L. R., 2012, *Science*, 337, 721
- Bergin E. A., Neufeld D. A., Melnick G. J., 1999, *ApJ*, 510, L145
- Beuther H., Churchwell E. B., McKee C. F., Tan J. C., 2007, in Reipurth B., Jewitt D., Keil K., eds, *Protostars and Planets V*. Univ. Arizona Press, Tucson, p. 165
- Bockelée-Morvan D. et al., 1998, *Icarus*, 133, 147
- Bockelée-Morvan D. et al., 2012, *A&A*, 544, L15
- Campins H. et al., 2010, *Nature*, 464, 1320
- Caselli P., Myers P. C., 1995, *ApJ*, 446, 665
- Caselli P., Hasegawa T. I., Herbst E., 1998, *ApJ*, 495, 309
- Caselli P. et al., 2012, *ApJ*, 759, L37
- Cazaux S., Caselli P., Spaans M., 2011, *ApJ*, 741, L34
- Ceccarelli C., Castets A., Caux E., Hollenbach D., Loinard L., Molinari S., Tielens A. G. G. M., 2000, *A&A*, 355, 1129
- Chavarría L. et al., 2010, *A&A*, 521, L37
- Comito C. et al., 2010, *A&A*, 521, L38
- Coutens A. et al., 2012, *A&A*, 539, A132
- Coutens A. et al., 2013a, *A&A*, 553, A75
- Coutens A. et al., 2013b, *A&A*, 560, A39
- Daniel F., Dubernet M.-L., Grosjean A., 2011, *A&A*, 536, A76
- De Buizer J. M., Radomski J. T., Telesco C. M., Piña R. K., 2003, *ApJ*, 598, 1127
- de Graauw T. et al., 2010, *A&A*, 518, L6
- Dislaire V., Hily-Blant P., Faure A., Maret S., Bacmann A., Pineau Des Forêts G., 2012, *A&A*, 537, A20
- Dos Santos S. F., Kokoouline V., Greene C. H., 2007, *J. Chem. Phys.*, 127, 124309
- Dulieu F., Amiaud L., Congiu E., Fillion J.-H., Matar E., Momeni A., Pirronello V., Lemaire J. L., 2010, *A&A*, 512, A30
- Emprechtinger M. et al., 2013, *ApJ*, 765, 61
- Faure A., Wiesenfeld L., Scribano Y., Ceccarelli C., 2012, *MNRAS*, 420, 699
- Flagey N. et al., 2013, *ApJ*, 762, 11
- Flower D. R., Pineau des Forêts G., Walmsley C. M., 2004, *A&A*, 427, 887

- Flower D. R., Pineau des Forêts G., Walmsley C. M., 2006a, *A&A*, 449, 621
- Flower D. R., Pineau des Forêts G., Walmsley C. M., 2006b, *A&A*, 456, 215
- Fraser H. J., Collings M. P., McCoustra M. R. S., Williams D. A., 2001, *MNRAS*, 327, 1165
- Furuya K., Aikawa Y., Tomida K., Matsumoto T., Saigo K., Tomisaka K., Hersant F., Wakelam V., 2012, *ApJ*, 758, 86
- Garay G., Reid M. J., Moran J. M., 1985, *ApJ*, 289, 681
- Garay G., Rodriguez L. F., van Gorkom J. H., 1986, *ApJ*, 309, 553
- Gaume R. A., Fey A. L., Claussen M. J., 1994, *ApJ*, 432, 648
- Gensheimer P. D., Mauersberger R., Wilson T. L., 1996, *A&A*, 314, 281
- Gerin M. et al., 2010, *A&A*, 521, L16
- Gerner T., Beuther H., Semenov D., Linz H., Vasyunina T., Bihr S., Shirley Y. L., Henning T., 2014, *A&A*, 563, A97
- Goldsmith P. F., Langer W. D., 1999, *ApJ*, 517, 209
- Hartogh P. et al., 2011, *Nature*, 478, 218
- Hasegawa T. I., Herbst E., 1993, *MNRAS*, 261, 83
- Hasegawa T. I., Herbst E., Leung C. M., 1992, *ApJS*, 82, 167
- Hatchell J., Thompson M. A., Millar T. J., MacDonald G. H., 1998, *A&AS*, 133, 29
- Hatchell J., Fuller G. A., Millar T. J., 2001, *A&A*, 372, 281
- Herpin F. et al., 2012, *A&A*, 542, A76
- Hersant F., Wakelam V., Dutrey A., Guilloteau S., Herbst E., 2009, *A&A*, 493, L49
- Hincelin U., Wakelam V., Hersant F., Guilloteau S., Loison J. C., Honvault P., Troe J., 2011, *A&A*, 530, A61
- Hogerheijde M. R., van der Tak F. F. S., 2000, *A&A*, 362, 697
- Hogerheijde M. R. et al., 2011, *Science*, 334, 338
- Hollenbach D., Kaufman M. J., Bergin E. A., Melnick G. J., 2009, *ApJ*, 690, 1497
- Honvault P., Jorfi M., González-Lezana T., Faure A., Pagani L., 2011a, *Phys. Rev. Lett.*, 107, 023201
- Honvault P., Jorfi M., González-Lezana T., Faure A., Pagani L., 2011b, *Phys. Chem. Chem. Phys.*, 13, 19089
- Hugo E., Asvany O., Schlemmer S., 2009, *J. Chem. Phys.*, 130, 164302
- Ioppolo S., Cuppen H. M., Romanzin C., van Dishoeck E. F., Linnartz H., 2008, *ApJ*, 686, 1474
- Jacq T., Henkel C., Walmsley C. M., Jewell P. R., Baudry A., 1988, *A&A*, 199, L5
- Jacq T., Walmsley C. M., Henkel C., Baudry A., Mauersberger R., Jewell P. R., 1990, *A&A*, 228, 447
- Jensen M. J., Bilodeau R. C., Safvan C. P., Seiersen K., Andersen L. H., Pedersen H. B., Heber O., 2000, *ApJ*, 543, 764
- Jørgensen J. K., van Dishoeck E. F., 2010, *ApJ*, 710, L72
- Kong S., Caselli P., Tan J. C., Wakelam V., 2013, *ApJ*, preprint ([arXiv:1312.0971](https://arxiv.org/abs/1312.0971))
- Kristensen L. E. et al., 2010, *A&A*, 521, L30
- Kristensen L. E. et al., 2012, *A&A*, 542, A8
- Kuchar T. A., Bania T. M., 1994, *ApJ*, 436, 117
- Küppers M. et al., 2014, *Nature*, 505, 525
- Lis D. C. et al., 2010, *A&A*, 521, L26
- Lis D. C. et al., 2013, *ApJ*, 774, L3
- Liu F., Parise B., Kristensen L., Visser R., van Dishoeck E. F., Güsten R., 2011, *A&A*, 527, A19
- Liu T., Wu Y., Zhang H., 2013a, *ApJ*, 776, 29
- Liu F.-C., Parise B., Wyrowski F., Zhang Q., Güsten R., 2013b, *A&A*, 550, A37
- McCall B. J. et al., 2004, *Phys. Rev. A*, 70, 052716
- MacDonald G. H., Gibb A. G., Habing R. J., Millar T. J., 1996, *A&AS*, 119, 333
- Marquette J. B., Rebrion C., Rowe B. R., 1988, *J. Chem. Phys.*, 89, 2041
- Miyauchi N., Hidaka H., Chigai T., Nagaoka A., Watanabe N., Kouchi A., 2008, *Chem. Phys. Lett.*, 456, 27
- Mokrane H., Chaabouni H., Accolla M., Congiu E., Dulieu F., Chehrouri M., Lemaire J. L., 2009, *ApJ*, 705, L195
- Mookerjee B., Casper E., Mundy L. G., Looney L. W., 2007, *ApJ*, 659, 447
- Mottram J. C., van Dishoeck E. F., Schmalzl M., Kristensen L. E., Visser R., Hogerheijde M. R., Bruderer S., 2013, *A&A*, 558, A126
- Müller H. S. P., Thorwirth S., Roth D. A., Winniewisser G., 2001, *A&A*, 370, L49
- Müller H. S. P., Schlöder F., Stutzki J., Winniewisser G., 2005, *J. Mol. Structure*, 742, 215
- Neill J. L., Wang S., Bergin E. A., Crockett N. R., Favre C., Plume R., Melnick G. J., 2013, *ApJ*, 770, 142
- Oba Y., Miyauchi N., Hidaka H., Chigai T., Watanabe N., Kouchi A., 2009, *ApJ*, 701, 464
- Öberg K. I., Linnartz H., Visser R., van Dishoeck E. F., 2009, *ApJ*, 693, 1209
- Ossenkopf V., Henning T., 1994, *A&A*, 291, 943
- Ott S., 2010, in Mizumoto Y., Morita K.-I., Ohishi M., eds, *ASP Conf. Ser. Vol. 434, Astronomical Data Analysis Software and Systems XIX*. Astron. Soc. Pac., San Francisco, p. 139
- Pagani L., Salez M., Wannier P. G., 1992, *A&A*, 258, 479
- Pagani L. et al., 2009, *A&A*, 494, 623
- Pardo J. R., Cernicharo J., Herpin F., Kawamura J., Kooi J., Phillips T. G., 2001, *ApJ*, 562, 799
- Parise B. et al., 2005, *A&A*, 431, 547
- Persson C. M. et al., 2007, *A&A*, 476, 807
- Persson M. V., Jørgensen J. K., van Dishoeck E. F., 2012, *A&A*, 541, A39
- Persson M. V., Jørgensen J. K., van Dishoeck E. F., 2013, *A&A*, 549, L3
- Persson M. V., Jørgensen J. K., van Dishoeck E. F., Harsono D., 2014, *A&A*, 563, A74
- Pickett H. M., Poynter R. L., Cohen E. A., Delitsky M. L., Pearson J. C., Müller H. S. P., 1998, *J. Quant. Spectrosc. Radiat. Transf.*, 60, 883
- Pilbratt G. L. et al., 2010, *A&A*, 518, L1
- Prasad S. S., Tarafdar S. P., 1983, *ApJ*, 267, 603
- Reid M. J., Ho P. T. P., 1985, *ApJ*, 288, L17
- Roberts H., Herbst E., 2002, *A&A*, 395, 233
- Roelfsema P. R. et al., 2012, *A&A*, 537, A17
- Rolfs R. et al., 2010, *A&A*, 521, L46
- Semenov D. et al., 2010, *A&A*, 522, A42
- Sewilo M., Churchwell E., Kurtz S., Goss W. M., Hofner P., 2004, *ApJ*, 605, 285
- Sewilo M., Churchwell E., Kurtz S., Goss W. M., Hofner P., 2011, *ApJS*, 194, 44
- Shen C. J., Greenberg J. M., Schutte W. A., van Dishoeck E. F., 2004, *A&A*, 415, 203
- Sipilä O., Caselli P., Harju J., 2013, *A&A*, 554, A92
- Sridharan T. K., Beuther H., Saito M., Wyrowski F., Schilke P., 2005, *ApJ*, 634, L57
- Taquet V., Peters P. S., Kahane C., Ceccarelli C., López-Sepulcre A., Toubin C., Dufrot D., Wiesenfeld L., 2013, *A&A*, 550, A127
- Taquet V., Charnley S. B., Sipilä O., 2014, *ApJ*, 791, 1
- Tielens A. G. G. M., Hagen W., 1982, *A&A*, 114, 245
- Turner B. E., Balick B., Cudaback D. D., Heiles C., Boyle R. J., 1974, *ApJ*, 194, 279
- van der Tak F. F. S., Walmsley C. M., Herpin F., Ceccarelli C., 2006, *A&A*, 447, 1011
- van der Tak F. F. S. et al., 2013, *A&A*, 554, A83
- van Dishoeck E. F., Herbst E., Neufeld D. A., 2013, *Chem. Rev.*, 113, 9043
- Wakelam V., Herbst E., Le Bourlot J., Hersant F., Selsis F., Guilloteau S., 2010, *A&A*, 517, A21
- Wakelam V., Vastel C., Aikawa Y., Coutens A., Bottinelli S., Caux E., 2014, *MNRAS*, submitted
- Walmsley C. M., Pineau des Forêts G., 2004, *A&A*, 418, 1035
- Watanabe N., Kouchi A., 2008, *Progress Surface Sc.*, 83, 439
- Watt S., Mundy L. G., 1999, *ApJS*, 125, 143
- Wilson T. L., 1999, *Rep. Progress Phys.*, 62, 143
- Wood D. O. S., Churchwell E., 1989, *ApJS*, 69, 831
- Wyrowski F., Güsten R., Menten K. M., Wiesemeyer H., Klein B., 2012, *A&A*, 542, L15
- Zinnecker H., Yorke H. W., 2007, *ARA&A*, 45, 481

SUPPORTING INFORMATION

Additional Supporting Information may be found in the online version of this article:

Appendix A. Herschel/HIFI Observations

Appendix B. Non-LTE Spherical Radiative Transfer Modeling

Appendix C. Sensitivity of our Modeling to the Inclusion of Spin-State Chemistry (<http://mnras.oxfordjournals.org/lookup/suppl/doi:10.1093/mnras/stu1816/-/DC1>).

Please note: Oxford University Press is not responsible for the content or functionality of any supporting materials supplied by the authors. Any queries (other than missing material) should be directed to the corresponding author for the article.

This paper has been typeset from a $\text{\TeX}/\text{\LaTeX}$ file prepared by the author.